



# Derivation of neutrino fluxes in Gamma-ray bursts using the multi-shell internal shock model

*Author:*

Filip Samuelsson (901022-3551)  
`filipsam@kth.se`

Department of Physics  
KTH Royal Institute of Technology

*Supervisor:* Damien Bégué

May 24, 2017

Typeset in L<sup>A</sup>T<sub>E</sub>X

TRITA-FYS 2017:37  
ISSN 0280-316X  
ISRN KTH/FYS/--17:37-SE

©Filip Samuelsson, May 24, 2017

## Abstract

In this thesis, I study five different benchmark Gamma-ray bursts and predict the resulting neutrino fluxes for each. I use the multi-shell internal shock model, following a paper published by Bustamante et al. (2016) [17]. The secondary particle distributions are calculated with a semi-analytical model instead of using a Monte-Carlo simulation software, following a procedure outline by Hümmer et al. (2010) [8]. The final all sky flux predictions are compared to IceCube's recently published upper limit [4]. Three out of five Gamma-ray bursts predict neutrino fluxes so high, that they can be discarded by the IceCube upper limit at a 90 % CL. By varying the energy fractions given to protons, electrons, and magnetic field, I find that the fluxes can be decreased below the upper bound.

## Sammanfattning

I denna avhandling studerar jag fem olika modell-gammablixtar (eng. Gamma-ray bursts) och förutsäger det resulterande neutrinoflödet. Jag använder multi-skal interna stöt modellen, följandes en artikel publicerad av Bustamante et al. (2016) [17]. De resulterande partikeldistributionerna är framtagna med hjälp av en semi-analytisk modell istället för via en Monte-Carlo simulation, via en procedur beskriven av Hümmer et al. (2010) [8]. De slutgiltiga förutsägelseerna av de himlatäckande flödena jämförs med IceCubes nya övre gränsvärde [4]. Tre av fem gammablixtar förutsäger neutrinoflöden som är så höga, att de kan förkastas med hjälp av IceCubes övre gräns med 90 % konfidensintervall. Genom att variera bråkdelen energi given till protoner, elektroner och magnetiskt fält, fann jag att flödena kunde minska under gränsvärdet.

# Contents

<b>1</b>	<b>Introduction</b>	<b>3</b>
1.1	Purpose . . . . .	4
1.2	Outline of the Thesis . . . . .	4
1.3	Author's Contribution . . . . .	4
<b>2</b>	<b>Background information</b>	<b>5</b>
2.1	Internal shock model . . . . .	5
2.2	Photosphere . . . . .	6
2.3	Neutrino production chain . . . . .	7
<b>3</b>	<b>Pion spectra</b>	<b>8</b>
3.1	Interactions considered and chapter outline . . . . .	8
3.2	Photon energy in the proton rest frame . . . . .	9
3.3	Pion production rate . . . . .	10
3.4	Interaction rate probability . . . . .	11
3.5	Pion distribution term . . . . .	12
3.6	Common to all production channels . . . . .	12
3.7	Three different production channels . . . . .	12
3.8	Resonances . . . . .	13
3.9	Direct production . . . . .	16
3.10	Multipion production . . . . .	19
<b>4</b>	<b>Neutrino spectra</b>	<b>21</b>
4.1	Synchrotron cooling . . . . .	21
4.2	Neutrino distribution . . . . .	24
4.3	Neutrino oscillations . . . . .	25
<b>5</b>	<b>Simulation outline</b>	<b>27</b>
5.1	Burst setup . . . . .	27
5.1.1	Initial Lorentz factors . . . . .	27
5.1.2	Initial masses . . . . .	28
5.1.3	Initial widths and shell distances . . . . .	28
5.1.4	Initial radii . . . . .	28
5.2	Burst evolution . . . . .	30
5.3	Control of the code . . . . .	32
5.4	Observation . . . . .	33
5.4.1	Observation time . . . . .	33
5.4.2	Energy output normalization . . . . .	34

5.4.3	Proton and photon distributions . . . . .	36
5.4.4	Obtaining neutrino spectra . . . . .	37
5.4.5	Implemented photosphere . . . . .	39
5.4.6	Gamma-ray pulse per collision and observed light curve . . . . .	40
<b>6</b>	<b>Results and discussion</b>	<b>43</b>
6.1	Results . . . . .	43
6.2	Discussion . . . . .	50
6.2.1	Energy scaling and initial $\Gamma$ spread . . . . .	50
6.2.2	Effects of subphotospheric collisions . . . . .	50
6.2.3	External contributions . . . . .	53
6.2.4	Varying assumptions . . . . .	53
6.2.5	Secondary photohadronic interactions and kaon decay . . . . .	54
<b>7</b>	<b>Conclusion</b>	<b>56</b>
<b>8</b>	<b>Acknowledgments</b>	<b>57</b>
<b>A</b>	<b>Justification of arbitrary initial kinetic energy</b>	<b>61</b>
	<b>Bibliography</b>	<b>63</b>

# Chapter 1

## Introduction

The most luminous events that we know of in the entire universe are gamma-ray bursts (GRBs). GRBs are so energetic that when one occurs, it can briefly outshine its entire host galaxy. They were first discovered in 1967 by the satellite Vela 4, a satellite launched by the Americans during the cold war whose mission it was to observe if the Russians did any illegal nuclear bomb testing. The Vela missions did detect something, but the data did not match that of a nuclear bombing. What they had recorded was extremely high energetic photons coming from outer space; the first GRB had been discovered [1].

When these observations were finally revealed to the public, it resulted in a lot of different ideas and speculations. Since then, much more data has been acquired, which has greatly increased our understanding. GRBs are an incredible energy release during a short period of time that we detect as high energy  $\gamma$ -rays, as well as other frequency radiation. They are fascinating, because they are very diverse in their behavior, and this has made them very difficult to categorize. In 1993 however, it was shown that they are bimodal in duration [2]. Less than one fourth of GRBs are short (SGRBs) [3], defined as shorter than 2 seconds in duration, while the rest are long GRBs (LGRBs) with duration ranging from 2 seconds up to several hours. It is now firmly believed that these two types have different physical progenitors, meaning that they are caused by different phenomenon. LGRBs have been linked to supernovae (SNe) of type Ib/c where the parent star has collapsed into a black hole, while the SGRBs are believed to be caused by merging neutron stars with either another neutron star (NS-NS) or with a black hole (NS-BH), but this is still being debated [3]. Due to LGRBs being both more common and longer, they have been studied more closely than SGRBs. In this thesis, I will focus only on LGRB (which will here on out be referred to as simply GRBs), even though much of the process could be applied to SGRB.

Although GRBs have been studied for several decades now, there is still no general consensus on a complete physical picture. One of the historically most popular models has been the internal shock model. While it has several advantages that lead it to its initial popularity, it also has major problems. One of these problems is that the internal shock model is predicted to produce a huge flux of neutrinos. So far, this signal has not been detected and neutrino telescopes such as the IceCube neutrino observatory keep on lowering the upper limits on neutrino fluxes from GRBs [4].

## 1.1 Purpose

The purpose of this thesis, is to make detailed predictions of the neutrino fluxes in the multi-shell internal shock model for five benchmark GRBs, and to compare these to newly released IceCube data [4], to see if the predicted fluxes are above or below their upper limit.

## 1.2 Outline of the Thesis

The thesis will begin by supplying the reader with necessary background information, so that what follows is more easily understood. Following the background chapter are two chapters in which I outline how to obtain a neutrino spectrum from general proton and photon spectra. This procedure has naturally been divided into two chapters, because roughly one half of the process lies in obtaining the pion spectra, treated in chapter 3, while the other half is obtaining the neutrino spectrum from the decaying pions, treated in chapter 4.

The simulation of the multi-shell GRBs, together with how all results are calculated, will be described in chapter 5. The results are shown in chapter 6, together with a discussion section on how the work could be refined. A final conclusion is presented in chapter 7.

## 1.3 Author's Contribution

All plots and figures were made by the author. In the case they have been reproduced from or inspired by someone else's work, this is clearly stated. The results obtained, the making of the simulation and the writing of the thesis are all the author's own original work.

# Chapter 2

## Background information

This chapter will focus on supplying the reader with some necessary background information. The following two sections on the internal shock model and the photosphere of a GRB only gives some basic information, and I urge the curious reader to look into one of the many good reviews about GRBs and ongoing research, for instance [3] by Asaf Pe'er (2016).

### 2.1 Internal shock model

There is disagreement in the scientific community about several things regarding GRBs. There is for instance much debate as to what process accelerates the outflows in the jet to such relativistic speeds. Furthermore, it is unclear how the kinetic energy is converted into the high energy radiation that we detect. Without caring about the process behind jet acceleration, (possibly due to magnetohydrodynamic acceleration, [5]), the internal shock model predicts that it is collisions between different regions in the jet that dissipates the kinetic energy, which thereafter is radiated away by synchrotron radiation and inverse Compton emission.

In the initial stages, close to the progenitor, fluctuations will be flattened out by interactions within the ejecta, but after a certain distance there will be different regions of the ejecta that are too far apart to influence one another. These regions, called shells, can have different properties such as different bulk Lorentz factors  $\Gamma$  and different masses. If the difference in  $\Gamma$  between two subsequent shells is large enough, effective energy conversion is possible [3].

As mentioned in the introduction, GRBs are very diverse. This can be seen from the different light curves in figure 1 in [3]. The light curves seem to come in all different shapes: some have a quick rise followed by an exponential decay, some have one, two, or more delta spikes, while yet others have what seems like completely random and chaotic behavior. To find a model that can mimic all these shapes has proven difficult. Here, the internal shock model has been successful in reproducing a wide variety of observed shapes. Because of this, together with a plausible explanation for efficient energy conversion and other reasons, the internal shock model has long been a favorite amongst scientists as the main process behind GRBs prompt emission. However, there are several drawbacks. One of the biggest is that for a GRB to acquire the high efficiency that is observed, the spread in initial  $\Gamma$  has to be very high, a spread which is difficult to explain with realistic progenitors [3, 6]. Another large drawback is that the predicted neutrino flux is so high,

that neutrino telescopes such as IceCube should have picked up a signal by now. This thesis will focus on the latter of these problems, although the efficiency problem will be briefly discussed in section 6.2.1.

## 2.2 Photosphere

Due to the extreme energy outburst in the central engine of a GRB, the temperature is initially high enough for pair production to occur. In the first phase, photons will interact strongly with the electrons associated with baryons, and the produced electrons and positrons; the plasma is optically thick. As the fireball keeps expanding, the temperature drops and electrons and positrons recombine. At some point in the expansion, the plasma will become optically thin, which means that the optical depth  $\tau$  will drop below one and photons can escape the plasma and reach earth. The radius at which this transition occurs is called the photospheric radius  $r_{\text{ph}}$ . Of course, the probability for a photon escaping the plasma is never none-zero, no matter how large  $\tau$  is, just as a photon created above the photospheric radius might scatter. The spectra observed at earth is a superposition of all these photons. In this thesis however, I have used the simplification to discard all photons created at  $r < r_{\text{ph}}$ , and account for all photons created at  $r > r_{\text{ph}}$ . The implication of this simplification is discussed in section 6.2.2.

The derivation to find the expression of the photosphere will follow the one in chapter 3.2.5 in [3]. The optical depth in the radial direction is given by

$$\tau = \int_r^\infty n'_e \sigma_T \Gamma (1 - \beta \cos \theta) dr', \quad (2.1)$$

where  $n'_e$  is the comoving electron density,  $\sigma_T$  is the Thomson cross section,  $\Gamma$  is the bulk Lorentz factor of the outflow,  $\theta$  is the angle to the line of sight, and  $\beta$  is the outflow velocity. The integral is over radial distance. When the photons decouple at the photosphere, the temperature have dropped below the pair production temperature, and the electron number density will be dominated by electrons associated with protons, i.e.,  $n'_e \approx n'_p$ . The number density of protons is given by the mass ejection rate  $\dot{M}$  divided by proton mass and volume as

$$n'_p \approx \frac{\dot{M}}{4\pi m_p r^2 c \Gamma}, \quad (2.2)$$

where the width of the ejecta is the length it reaches per second, which is  $v' = v\Gamma \approx c\Gamma$ . Inserting the expression above into equation (2.1) and rewriting  $(1 - \beta) = (2\Gamma^2)^{-1}$  one gets

$$\tau = \frac{\dot{M} \sigma_T}{8\pi m_p r c \Gamma^2}, \quad (2.3)$$

after integration and approximating  $\cos \theta = 1$  (radiation traveling along the line of sight). The photospheric radius is defined as  $\tau(r_{\text{ph}}) \equiv 1$  and so one gets the expression for the photospheric radius as

$$r_{\text{ph}} = \frac{\dot{M} \sigma_T}{8\pi m_p c \Gamma^2}. \quad (2.4)$$

## 2.3 Neutrino production chain

In the collisions between the different shells of the outflow, there will be huge amounts of energy released. This energy will first raise the internal energy of the shell and generate a magnetic field over the shock. Particles will be accelerated in the created magnetic field and the excess energy will soon be lost due to the synchrotron cooling of the accelerated particles. After a collision, there will be high energy protons and photons in abundance in the shell. In the inevitable high energy photohadronic interactions (interactions between photons and hadrons),  $\pi^0$ ,  $\pi^+$ , and  $\pi^-$  will be produced. Neutrinos are then produced in the decay chain of the charged pions:

$$\begin{aligned}\pi^+ &\rightarrow \mu^+ + \nu_\mu, \\ \mu^+ &\rightarrow e^+ + \nu_e + \bar{\nu}_\mu,\end{aligned}\tag{2.5}$$

and

$$\begin{aligned}\pi^- &\rightarrow \mu^- + \bar{\nu}_\mu, \\ \mu^- &\rightarrow e^- + \bar{\nu}_e + \nu_\mu.\end{aligned}\tag{2.6}$$

Therefore, to predict the neutrino flux, one first has to obtain the pion distribution. The neutral pions most common decay is

$$\pi^0 \rightarrow 2\gamma\tag{2.7}$$

with a branching ratio of 98.8 %, and less than 0.1 % of all  $\pi^0$  decays result in neutrino production [7]. Therefore, the contribution from neutral pions can safely be neglected in this work.

# Chapter 3

## Pion spectra

The simulation, outlined in chapter 5, will produce proton and photon distributions for each shell collision in the simulated GRB. In high energy photohadronic interactions,  $\pi^0$ ,  $\pi^+$ , and  $\pi^-$  are produced, and neutrinos are produced in the subsequent decay of the charged pions. Thus, the scheme will be to first acquire the pion distribution in this chapter, and thereafter get the neutrino spectra in chapter 4.

Calculating the neutrino spectra from a given proton  $p$  and photon  $\gamma$  distribution is no trivial task. This chapter and the next will describe the procedure in detail. I have decided not to work in a Monte Carlo simulation program to generate the secondary particle spectra, but rather use a semi-analytical approach. The advantage of this is that it gives more insight of the different contributions and what assumptions are viable and not. It is also much faster than a full scale Monte Carlo simulation.

The procedure is taken from a paper by Hümmer et al. (2010) [8]. In it, they describe both full scale and simplified methods of obtaining the neutrinos. Their paper has been followed in detail and when necessary, I indicate which method I have used to avoid ambiguity. They have in turn followed the code behind a Monte Carlo simulation software called SOPHIA (Simulations Of Photo Hadronic Interactions in Astrophysics) [9] developed as a tool for problems involving photohadronic interactions in an astrophysical setting. Hümmer et al. (2010) have made simplifications to make an analytical approach possible. The procedure outlined in this chapter is general and can be applied to arbitrary  $p$  and  $\gamma$  distributions.

In this chapter and the next, I will work mainly in the shock rest frame (SRF) as opposed to the observer frame (OF). However, keep in mind that the resulting neutrino spectra obtained are in the SRF, and need to be Lorentz boosted into the OF.

### 3.1 Interactions considered and chapter outline

High energy photohadronic interactions can create pions through several different interactions. While there are simplifications where one only account for the lowest  $\Delta$ -resonance interaction, (see equation (1) in Hummer et al. (2010) [8]) I have decided to use a more accurate and refined approach to calculate the pion spectra. This makes it possible to differentiate between neutrinos and antineutrinos and different neutrino flavors in the end, as well as the possibility to predict the shape of the neutrino distribution. The cost of this accuracy is transparency and simplicity, and this section will focus on explaining the procedure as simply as possible.

The contribution to neutrino production from  $pp$  collision will not be considered. Even though the cross section for  $pp$  interaction is larger than for  $p\gamma$ , the density of protons in the ejecta is so much lower than the photon density, that  $p\gamma$  collisions outnumber  $pp$  collisions by at least two orders of magnitude [10,11]. Furthermore, I have not included kaon decay, as its effect on the final peak height of the neutrino fluxes is relatively small [8].

In sections 3.2 - 3.6, I will derive a formula for pion production, that is general for all different pion production channels. In section 3.7, I will describe the three production channels treated in this thesis: resonances, including higher resonances, direct production (t-channel), and multipion production. The last three sections will focus on each of these production channels in turn.

## 3.2 Photon energy in the proton rest frame

The cross sections for all different interactions are more easily expressed as a function of photon energy the proton rest frame (PRF),  $\epsilon_r$ , while my simulation will generate the proton and photon energy distributions in the SRF. To proceed, it is therefore necessary to have an expression for  $\epsilon_r$  in terms of  $E$ , the proton energy in the SRF, and  $\epsilon$ , the photon energy in the SRF. This can be obtained using the equality of four-momentum squared in the SRF and the PRF:

$$(p_p + p_\gamma)_{\text{SRF}}^2 = (p_p + p_\gamma)_{\text{PRF}}^2. \quad (3.1)$$

In the SRF, the proton and the photon have four-momenta

$$p_{p,\text{SRF}} = \gamma_p \left( m_p c, m_p \bar{v}_p \right)_{\text{SRF}}, \quad p_{\gamma,\text{SRF}} = \left( \frac{\epsilon}{c}, \frac{\epsilon \bar{v}_\gamma}{c^2} \right)_{\text{SRF}},$$

where  $m_p$  is proton mass,  $c$  is the speed of light in vacuum, and  $\bar{v}_i$  is the velocity of particle  $i$ . The sum of their four momenta squared is

$$\begin{aligned} (p_p + p_\gamma)_{\text{SRF}}^2 &= p_p^2 + p_\gamma^2 + 2p_p p_\gamma = \\ &= m_p^2 c^2 + 0 + 2 \left( \gamma_p m_p c \frac{\epsilon}{c} - \gamma_p m_p \bar{v}_p \cdot \frac{\epsilon \bar{v}_\gamma}{c^2} \right), \end{aligned} \quad (3.2)$$

which, with  $\bar{v}_p \cdot \bar{v}_\gamma = v_p c \cos \theta$  becomes

$$(p_p + p_\gamma)_{\text{SRF}}^2 = m_p^2 c^2 + 2\gamma_p m_p \epsilon (1 - \beta_p \cos \theta). \quad (3.3)$$

This should be compared to the four-momenta squared in the PRF:

$$p_{p,\text{PRF}} = (m_p c, \bar{0})_{\text{PRF}}, \quad p_{\gamma,\text{PRF}} = \left( \frac{\epsilon_r}{c}, \frac{\epsilon_r \bar{v}_\gamma'}{c^2} \right)_{\text{PRF}}.$$

Their sum squared becomes

$$(p_p + p_\gamma)_{\text{PRF}}^2 = m_p^2 c^2 + 0 + 2m_p \epsilon_r, \quad (3.4)$$

Setting equation (3.3) and (3.4) equal yields

$$2\gamma_p m_p \epsilon (1 - \beta_p \cos \theta) = 2m_p \epsilon_r \quad (3.5)$$

which can be solved for  $\epsilon_r$  as

$$\epsilon_r = \gamma_p \epsilon (1 - \beta_p \cos \theta) \quad (3.6)$$

Finally, putting  $\gamma_p = E/(m_p c^2)$  one gets

$$\epsilon_r = \frac{E \epsilon}{m_p c^2} (1 - \beta_p \cos \theta) \approx \frac{E \epsilon}{m_p c^2} (1 - \cos \theta), \quad (3.7)$$

with  $\beta_p \approx 1$ .

### 3.3 Pion production rate

As mentioned,  $p\gamma$  interactions can produce pions in several different ways. For each interaction there are many things that contribute to the production rate. Considering pions created with final energy  $E_\pi$ , what factors need to be taken into account? Because the number of photons is much greater than the number of protons, the number of available protons  $N_p(E)$  that can produce a pion of energy  $E_\pi$  is one limiting factor. This factor must however be multiplied by a term  $dn_{E \rightarrow E_\pi}^{\text{IT}}/dE_\pi$ , which accounts for the distribution of pion energies a proton of energy  $E$  can produce. In more detail, a proton with energy  $E$  might be able to create a pion in a whole range of energies, where  $E_\pi$  is only one possibility. Therefore, only a fraction of the protons with energy  $E$  will actually create pions with energy  $E_\pi$ , and the term  $dn_{E \rightarrow E_\pi}^{\text{IT}}/dE_\pi$  generates this fraction. Furthermore, this term accounts for the fact that created pions have lower energies than their parent protons. The function  $dn_{E \rightarrow E_\pi}^{\text{IT}}/dE_\pi$  is a function of both the parent proton's and the daughter pion's energies. The last factor that contributes is the interaction rate probability per particle and unit time that a proton with energy  $E$  will interact with a photon and create a pion; if we don't take this term into account, it would indicate the number of created pions would equal the number of initial protons, which is obviously untrue. This term, we denote  $\Gamma_{p \rightarrow \pi}^{\text{IT}}$  and it is only a function of proton energy.

Putting these together, the number of pions created per energy and time for a specific interaction IT is given by

$$Q_\pi^{\text{IT}}(E_\pi) = \int_{E_\pi}^{\infty} dE N_p(E) \frac{dn_{E \rightarrow E_\pi}^{\text{IT}}(E, E_\pi)}{dE_\pi} \Gamma_{p \rightarrow \pi}^{\text{IT}}(E), \quad (3.8)$$

where the integral starts at  $E_\pi$ , as protons with  $E < E_\pi$  are assumed to be unable to create a pion with energy  $E_\pi$ . This is the pion production rate for interaction IT. To obtain the total number of pions produced, one has to integrate over time.

Equation (3.8) includes all pion species and gives you no information about the ratios between the species. Therefore, one needs to include the so called multiplicity  $M_{\pi^i}^{\text{IT}}$ , where  $i = 0, +, -$ . The multiplicity accounts for the ratio in which the species are created. For instance, consider the lowest  $\Delta$ -resonance

$$p + \gamma \rightarrow \Delta^+ \rightarrow \begin{cases} n + \pi^+ & 1/3 \text{ of the cases} \\ p + \pi^0 & 2/3 \text{ of the cases,} \end{cases} \quad (3.9)$$

where the proton interacts with the photon to create a  $\Delta^+$  baryon that subsequently decays in one of the two channels mentioned above. In this case, the reaction can yield a

$\pi^+$  or a  $\pi^0$  as end product and the multiplicity  $M_\pi^{\text{IT}}$  tells you how likely each branch is. The multiplicity is in general a function of energy as well, but in this thesis it will be taken as a constant, but will of course differ for different interaction. Thus, the production rate of a specific species  $i$  of pions is

$$Q_{\pi^i}^{\text{IT}}(E_\pi) = M_{\pi^i}^{\text{IT}} Q_\pi^{\text{IT}}(E_\pi), \quad (3.10)$$

where I have omitted an  $i$  as a superscript on  $E_\pi$ , as the species dependency is completely covered in  $M_{\pi,i}^{\text{IT}}$ . The total production rate of pions of pion species  $i$  is then obtained by summing over all different interactions:

$$Q_{\pi^i}(E_\pi) = \sum_{\text{IT}} M_{\pi^i}^{\text{IT}} \int_{E_\pi}^{\infty} dE N_p(E) \frac{dn_{E \rightarrow E_\pi}^{\text{IT}}(E, E_\pi)}{dE_\pi} \Gamma_{p \rightarrow \pi}^{\text{IT}}(E). \quad (3.11)$$

From this point on, the goal with this chapter is to obtain expression for these quantities, and to do so for each interaction.

### 3.4 Interaction rate probability

The interaction rate probability  $\Gamma_{p \rightarrow \pi}^{\text{IT}}(E)$  of a proton is dependent on its reaction partner, in this case the photon distribution, and the cross section for the interaction  $\sigma^{\text{IT}}$ . The cross sections are most easily expressed in the PRF, and it is therefore a function of  $\epsilon_r$ . But  $\epsilon_r$  is in turn dependent on both  $E$  and  $\varepsilon$ , as well as the angle  $\theta$  between their momenta in the SRF; a head on collision results in more available energy than a collision where the proton and photon have their momenta almost aligned. The interaction probability rate is therefore a double integral

$$\Gamma_{p \rightarrow \pi}^{\text{IT}}(E) = c \int d\varepsilon \int_{-1}^{+1} \frac{d \cos \theta}{2} (1 - \cos \theta) \times n_\gamma(\varepsilon, \cos \theta) \sigma^{\text{IT}}(\epsilon_r). \quad (3.12)$$

Please observe that primes are omitted, but that  $n_\gamma$  is in the SRF. The term  $c$  appears because the number of photons that the proton could possibly react with in a second is those within distance  $c$ .

For reasons that will soon become apparent, it is easier to rewrite the integral over  $\cos \theta$  as an integral over  $\epsilon_r$  instead, and this can be easily done. Equation (3.7) gives that

$$\begin{cases} \cos \theta = -1 & \rightarrow & \epsilon_r = \frac{2E\varepsilon}{m_p} \\ \cos \theta = 1 & \rightarrow & \epsilon_r = 0 \\ 1 - \cos \theta & = & \frac{\epsilon_r m_p}{E\varepsilon} \\ d \cos \theta & = & -\frac{m_p}{E\varepsilon} d\epsilon_r, \end{cases} \quad (3.13)$$

where  $m_p$  is in GeV (factor of  $c^2$  left out) and thus

$$\int_{-1}^{+1} \frac{d \cos \theta}{2} (1 - \cos \theta) = \frac{1}{2} \left( \frac{m_p}{E\varepsilon} \right)^2 \int_0^{\frac{2E\varepsilon}{m_p}} \epsilon_r d\epsilon_r, \quad (3.14)$$

where the minus sign from the derivative term has been canceled by switching the limits in the integral.

If one assumes an isotropic photon distribution in the SRF, then  $n_\gamma(\varepsilon, \cos \theta) = n_\gamma(\varepsilon)$  and the interaction rate probability is

$$\Gamma_{p \rightarrow \pi}^{\text{IT}}(E) = c \int d\varepsilon n_\gamma(\varepsilon) \times \frac{1}{2} \left( \frac{m_p}{E\varepsilon} \right)^2 \int_0^{\frac{2E\varepsilon}{m_p}} \epsilon_r d\epsilon_r \sigma^{\text{IT}}(\epsilon_r), \quad (3.15)$$

### 3.5 Pion distribution term

The pion distribution term  $dn_{E \rightarrow E_\pi}^{\text{IT}}/dE_\pi$  represents the probability for a pion with energy  $E_\pi$  to be created by a proton with energy  $E$ . I will make two assumptions. First, in the SRF the protons have much higher energies than the photons, and therefore the pion energy can be written as a fraction of the proton energy only,  $E_\pi = \chi^{\text{IT}}(\epsilon_r)E$ , where  $\chi^{\text{IT}}(\epsilon_r)$  is the mean fraction of proton energy received by the pion as a function of  $\epsilon_r$ . Secondly, I assume the pion distribution to be sufficiently peaked around the mean energy. In this case, the distribution can be approximated by a delta function

$$\frac{dn_{E \rightarrow E_\pi}^{\text{IT}}}{dE_\pi}(E, E_\pi) \simeq \delta(E_\pi - \chi^{\text{IT}}(\epsilon_r)E). \quad (3.16)$$

Although this will be a crucial simplification, the fraction  $\chi^{\text{IT}}(\epsilon_r)$  can be pretty complicated by itself.

### 3.6 Common to all production channels

The rate of pion production for a specific energy  $E_\pi$ , is given by inserting equations (3.15) and (3.16) into equation (3.11)

$$Q_\pi(E_\pi) = \int_{E_\pi}^{\infty} \frac{dE}{E} N_p(E) \cdot c \int_{\frac{\epsilon_{\text{th}} m_p}{2E}}^{\infty} d\varepsilon n_\gamma(\varepsilon) \times \sum_{\text{IT}} \frac{1}{2} \left( \frac{m_p}{E\varepsilon} \right)^2 \int_{\epsilon_{\text{th}}}^{\frac{2E\varepsilon}{m_p}} d\epsilon_r \epsilon_r \sigma^{\text{IT}}(\epsilon_r) M^{\text{IT}} \delta\left(\frac{E_\pi}{E} - \chi^{\text{IT}}(\epsilon_r)\right), \quad (3.17)$$

where the  $i$  indicating pion species has been dropped, as the theory is identical for all species. Observe that a factor of  $E^{-1}$  has appeared in the first integral, because of the division by  $E$  in the  $\delta$ -function. Furthermore, the lower limit in the integral over  $\epsilon_r$  is set to start at the threshold energy  $\epsilon_{\text{th}} = 150$  MeV below which the cross sections for all interactions are zero, and the lower limit in the photon integral has been set to match the lower limit of  $\epsilon_r$ .

The integral over  $\epsilon_r$  above was derived from an integral over interaction angle  $\theta$  in section 3.4. Thus, an interpretation for the  $\delta$ -function in the  $\epsilon_r$  integral is that, for each value of  $E_\pi$ ,  $E$ , and  $\varepsilon$  that are given, there will be a singular angle  $\theta$  with which the proton of incoming energy  $E$  could be reduced to a pion with energy  $E_\pi$ , under the conservation of linear momentum. This angle is transformed into a unique value in  $\epsilon_r$ .

### 3.7 Three different production channels

Everything described so far has been general and can be applied to all different interactions. To continue, it is necessary to look at the individual interactions themselves.

This section will list the three production channels for pions included in this thesis. These will in turn be divided further into different interactions. The three production channels are *Resonances*, *Direct production*, and *Multipion production*.

**Resonances.** Resonances are excited baryon states that often have short lifetimes. When they decay, they often produce pions. I take into account three different sub-interactions for resonances, which I will denote R1, R2, and R3.

The first of these, R1, produces one pion through

$$p + \gamma \xrightarrow{\Delta, N} p' + \pi, \quad (3.18)$$

where  $p'$  can be either a proton or a neutron, resulting in the creation of a  $\pi^0$  or a  $\pi^+$  respectively. Here,  $\Delta, N$  indicates that the reaction occurs through an virtual excited  $\Delta$  particle ( $\Delta$ -resonance) or excited nucleon ( $N$ -resonance)

The second one, R2, results in two created pions through the decay of a higher resonance into a pion plus a lower resonance, which in turn decays into a nucleon and a second pion through the decay chain

$$p + \gamma \xrightarrow{\Delta, N} \Delta' + \pi, \quad (3.19a)$$

$$\Delta' \rightarrow p' + \pi'. \quad (3.19b)$$

The energies of the two created pions will of course be different, and so they have different values of the fraction  $\chi$ . It is therefore easier to split the interaction into two parts and say that the first pion is created through interaction R2a and the second through R2b.

Lastly there is R3, which also creates two pions in total. In this case, the resonance creates a  $\rho$ -meson and a nucleon, and the  $\rho$ -meson then decays into two pions:

$$p + \gamma \xrightarrow{\Delta, N} \rho + p', \quad (3.20)$$

$$\rho \rightarrow \pi + \pi'.$$

**Direct production** The reactions described in equations (3.18) and (3.19) can also occur in the  $t$ -channel, through the direct exchange of a pion between the proton and the photon instead of through a virtual baryon resonance. These interactions, I will denote T1 and T2. The photon can only couple to the charged pions however, so for example for T1, only the reaction  $p + \gamma \rightarrow n + \pi^+$  is possible.

**Multipion production** For higher values of  $\epsilon_r$ , i.e., when there is more available energy, multipion production becomes the most important production channel. It is called multipion production because at high enough energies ( $\epsilon_r > 0.5$  GeV) QCD fragmentation becomes possible, creating jets of particles. This leads to several pions being created in each  $p\gamma$  interaction. There will be many interactions considered in this category, as explained in section 3.10 regarding multipion production.

For both direct production and multipion production, I will use approximative models. Why, and how these look will be described in their respective sections.

## 3.8 Resonances

The resonances are dealt with following chapter 3 in Hümmer et al. (2010) [8]. This is their most detailed approach for calculating resonances. It is the only one of the three

production channels that will be dealt with in such detail, the other two will be done using a simplified model in each case.

In  $p\gamma$ -interactions several different resonances are possible, depending on the incoming particles energies. In this thesis we will take into account nine different  $\Delta$ - and  $N$ -resonances, listed in Hümmer et al. (2010) table 2 [8].

Cross sections for photohadronic resonances, given in  $\mu\text{barn}$  below, are described by the Breit-Wigner formula. For the spin  $J$ , the nominal mass  $M$  and the width  $\Gamma$  of the resonance, it takes the expression

$$\begin{aligned}\sigma_{\text{BW}}^{\text{IT}} &= \frac{s}{(2m_p\epsilon_r)^2} \frac{4\pi(2J+1) B_\gamma B_{\text{out}} s \Gamma^2}{(s-M^2)^2 + s\Gamma^2} \\ &= B_{\text{out}}^{\text{IT}} \frac{s}{\epsilon_r^2} \frac{\sigma_0^{\text{IT}} (\Gamma^{\text{IT}})^2 s}{(s-(M^{\text{IT}})^2)^2 + (\Gamma^{\text{IT}})^2 s},\end{aligned}\tag{3.21}$$

where  $\sqrt{s}$  is the total CMF energy available, related to  $\epsilon_r$  as

$$s(\epsilon_r) = m_p^2 + 2m_p\epsilon_r.\tag{3.22}$$

the vector  $B_{\text{out}}^{\text{IT}}$  contains the fractions for each interaction R1, R2, and R3. (As an example, for the lowest resonance  $\Delta(1332)$  that can only interact through R1,  $B_{\text{out}}^{\text{IT}} = [1, 0, 0]$ ). The values of  $B_{\text{out}}^{\text{IT}}$ ,  $\sigma_0^{\text{IT}}$ ,  $\Gamma^{\text{IT}}$ , and  $M^{\text{IT}}$  are given constants, listed for each of the nine resonances in Hümmer et al. (2010) table 2 [8]. To account for phase-space reduction near the threshold, equation (3.21) has to be multiplied by a function  $R_{\text{th}}$ :

$$R_{\text{th}}^{\text{IT}} = \begin{cases} 0 & \text{if } \epsilon_r \leq \epsilon_{\text{th}}^{\text{IT}}, \\ \frac{\epsilon_r - \epsilon_{\text{th}}^{\text{IT}}}{w^{\text{IT}}} & \text{if } \epsilon_{\text{th}}^{\text{IT}} < \epsilon_r < w^{\text{IT}} + \epsilon_{\text{th}}^{\text{IT}}, \\ 1 & \text{if } \epsilon_r \geq w^{\text{IT}} + \epsilon_{\text{th}}^{\text{IT}}, \end{cases}\tag{3.23}$$

with  $\epsilon_{\text{th}}^{\text{IT}}$  and  $w^{\text{IT}}$  also listed in Hümmer et al. (2010) table 2 [8]. Thus, the cross section used for the resonances are

$$\sigma_{\text{R}}^{\text{IT}} = R_{\text{th}}^{\text{IT}} \cdot \sigma_{\text{BW}}^{\text{IT}}.\tag{3.24}$$

The cross sections for the nine different resonances and how they vary with energy can be seen in figure 3.1.

The function  $\chi^{\text{IT}}$  that appears in the delta function in equation (3.17) gives the fraction of the proton energy received by the pion. It is completely determined by the kinematics of the specific interaction and a derivation can be found in section 3.2 in [8]. The fraction  $\chi^{\text{IT}}$  for the different interactions are

Interaction R1:

$$\chi^1(\epsilon_r) = \frac{2m_p\epsilon_r + m_\pi^2}{4m_p\epsilon_r + 2m_p^2} (1 + \beta_\pi^{\text{CM}} \cos\theta_\pi)\tag{3.25}$$

Interaction R2a:

$$\chi^{2a}(\epsilon_r) = \frac{2m_p\epsilon_r + m_p^2 - m_\Delta^2 + m_\pi^2}{4m_p\epsilon_r + 2m_p^2} (1 + \beta_\pi^{\text{CM}} \cos\theta_\pi)\tag{3.26}$$

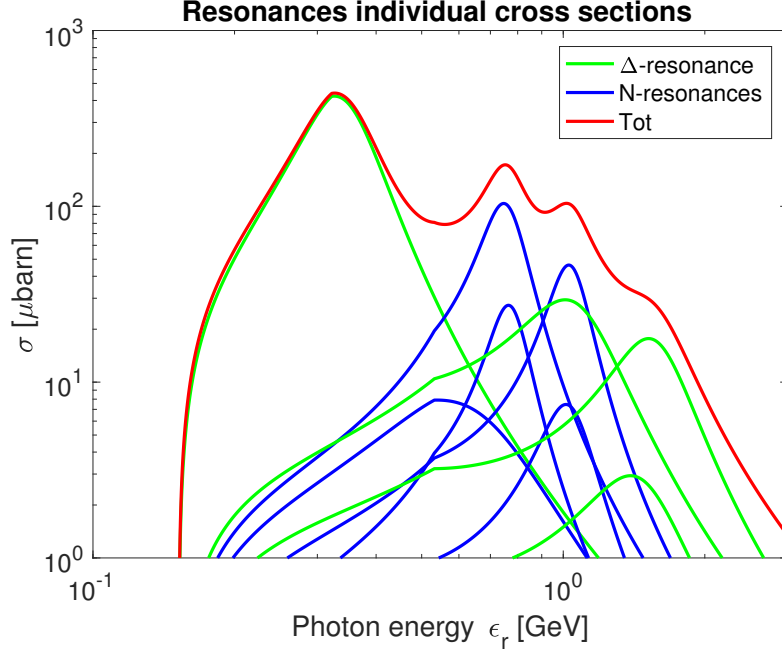


**Figure 3.1:** Cross sections as function of  $\epsilon_r$  for the nine different resonances. The green lines corresponds to  $\Delta$ -resonances and the blue to  $N$ -resonances. The red line is the total. Figure reproduced from Hümmer et al. (2010) [8].

Interaction R2b:

$$\chi^{2b}(\epsilon_r) = \frac{1}{2} \frac{2m_p\epsilon_r + m_p^2 - m_\pi^2 + m_\Delta^2}{4m_p\epsilon_r + 2m_p^2} \cdot \frac{m_\Delta^2 - m_p^2 + m_\pi^2}{2m_\Delta^2} (1 + \beta_\Delta^{\text{CM}} \cos \theta_\Delta) \quad (3.27)$$

Interaction R3:

$$\chi^3(\epsilon_r) = \frac{1}{2} \frac{2m_p\epsilon_r + m_\rho^2}{4m_p\epsilon_r + 2m_p^2} (1 + \beta_\Delta^{\text{CM}} \cos \theta_\Delta), \quad (3.28)$$

where the superscripts of  $\chi$  refers to the different interactions given in equations (3.18), (3.19), and (3.20) respectively. The other terms are:  $m_i$ , the mass of particle  $i$  with  $\Delta = \Delta(1232)$ ,  $\beta_i^{\text{CM}}$ , the speed of particle  $i$  in the center of mass frame (CMF), and  $\theta_i$ , the angle of emission for particle  $i$ . Note that all masses are given in GeV, and that both  $m_p$  and  $m_p$  appears in  $\chi^3(\epsilon_r)$ .

All resonances have to first approximation  $\langle \cos \theta_i \rangle \simeq 0$ , which simplifies the equations for  $\chi^{\text{IT}}$ . With this simplification, once can find  $\epsilon_r = \epsilon_{r,0}^{\text{IT}}$  that satisfy

$$\frac{E_\pi}{E} - \chi^{\text{IT}}(\epsilon_r) = 0. \quad (3.29)$$

From the properties of the Dirac  $\delta$ -function we know that if the  $\delta$ -function has a function  $g(x)$  as its argument, the following relation holds:

$$\delta(g(x)) = \sum_{x_0} \frac{\delta(x - x_0)}{|g'(x_0)|}, \quad (3.30)$$

where the sum is taken over all zeros of  $g(x)$ , i.e.,  $g(x_0) = 0$ , and  $|g'(x_0)|$  is the absolute value of the derivative evaluated at  $x_0$ . Labeling  $g^{\text{IT}}(\epsilon_r) = E_\pi/E - \chi^{\text{IT}}$ , the derivatives can

be computed from equations (3.25) - (3.28). Although rewriting it in the form requires computing the derivatives as well, one gains the great advantage of not having to evaluate the integral over  $\epsilon_r$ .

Inserting the different expressions for  $\chi$  given in equations (3.25) - (3.28) and putting  $\cos\theta_\pi = 0$ , the zeros of  $g^{\text{IT}}(\epsilon_r)$  are the following:

Interaction R1

$$\epsilon_{r,0}^1 = \frac{m_\pi^2 E - 2m_p^2 E_\pi}{4m_p E_\pi - 2m_p E}. \quad (3.31)$$

Interaction R2a

$$\epsilon_{r,0}^{2a} = \frac{E(m_p^2 + m_\pi^2 - m_\Delta^2) - 2m_p^2 E_\pi}{4m_p E_\pi - 2m_p E}. \quad (3.32)$$

Interaction R2b

$$\epsilon_{r,0}^{2b} = \frac{a \cdot E(m_p^2 + m_\pi^2 - m_\Delta^2) - 2m_p^2 E_\pi}{4m_p E_\pi - 2m_p E \cdot a}, \quad (3.33)$$

where  $a = \frac{m_\Delta^2 - m_p^2 + m_\pi^2}{2m_\Delta^2}$ .

Interaction R3

$$\epsilon_{r,0}^3 = \frac{m_\rho^2 E - 4m_p^2 E_\pi}{8m_p E_\pi - 2m_p E}. \quad (3.34)$$

The derivatives can also be computed from equations (3.25)-(3.28):

Interaction R1

$$g'^1(\epsilon_r) = -\frac{m_p^2 - m_\pi^2}{m_p(2\epsilon_r + m_p)^2}. \quad (3.35)$$

Interaction R2a

$$g'^{2a}(\epsilon_r) = -\frac{m_\Delta^2 - m_\pi^2}{m_p(2\epsilon_r + m_p)^2}. \quad (3.36)$$

Interaction R2b

$$g'^{2b}(\epsilon_r) = -\frac{m_\pi^2 - m_\Delta^2}{m_p(2\epsilon_r + m_p)^2} \cdot a, \quad (3.37)$$

where  $a = \frac{m_\Delta^2 - m_p^2 + m_\pi^2}{2m_\Delta^2}$ .

Interaction R3

$$g'^3(\epsilon_r) = -\frac{1}{2} \frac{m_p^2 - m_\rho^2}{m_p(2\epsilon_r + m_p)^2}. \quad (3.38)$$

With the cross section in equation (3.1), the  $\delta$ -function written as in equation (3.30), and the expressions for  $\epsilon_{r,0}^{\text{IT}}$  and  $g'^{\text{IT}}$  given above, the contribution from resonances is calculated using equation (3.17).

### 3.9 Direct production

The cross section for direct production is of course different from those of the resonances (see figure 3.2 for the energy dependence of the cross sections for the different production

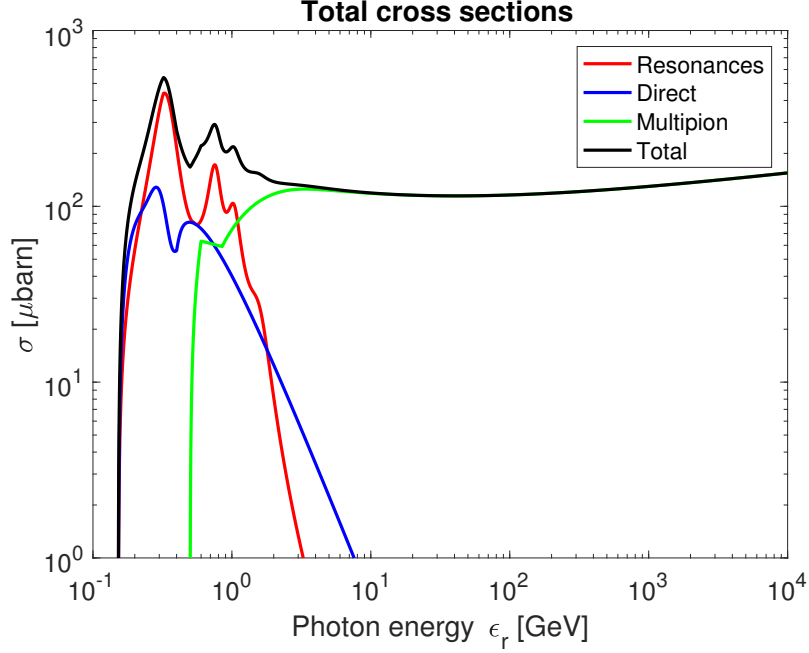


**Figure 3.2:** Energy dependence of  $\sigma$  for the different production channels. All interactions for each production channel have been summed to create the plot. Figure reproduced from Hümmer et al. (2010) [8].

channels). The cross sections for direct production are taken from SOPHIA [9] as

$$\sigma^{\text{T1}}(\epsilon_r) = \Theta(\epsilon_r - 0.152) \left[ 92.7 \text{Pl}(\epsilon_r, 0.152, 0.25, 2) + 40 \exp\left(-\frac{(\epsilon_r - 0.29)^2}{0.002}\right) - 15 \exp\left(-\frac{(\epsilon_r - 0.37)^2}{0.002}\right) \right] \quad (3.39)$$

with

$$\text{Pl}(\epsilon_r, \epsilon_{\text{th}}, \epsilon_{\text{max}}, \alpha) = \begin{cases} 0 & \text{if } \epsilon_r \leq \epsilon_{\text{th}}, \\ \left(\frac{\epsilon_r - \epsilon_{\text{th}}}{\epsilon_{\text{max}} - \epsilon_{\text{th}}}\right)^{\alpha(\epsilon_{\text{max}}/\epsilon_{\text{th}} - 1)} \left(\frac{\epsilon_r}{\epsilon_{\text{max}}}\right)^{-\alpha\epsilon_{\text{max}}/\epsilon_{\text{th}}} & \text{else,} \end{cases} \quad (3.40)$$

where  $\Theta(\epsilon_r - 0.152)$  is the Heaviside step function. This has been added by me (i.e. does not appear in the documentation for SOPHIA) to assure that the cross section goes to zero for small energies. For T2, the cross section is simply given by

$$\sigma^{\text{T2}}(\epsilon_r) = 37.7 \text{Pl}(\epsilon_r, 0.4, 0.6, 2). \quad (3.41)$$

The method described for resonances in the previous section can unfortunately not be used for direct production. The problem with this approach arises in the expression for  $\chi$ . For resonances,  $\langle \cos \theta_i \rangle \approx 0$  is a good approximation; all created pions travel more or less in the same direction as their parent proton in the CMF. This makes the resulting pion energy distribution more peaked around the mean value. However, this is not the case for direct production, as can be seen in figure 14 in [8]. The angle can to a

first approximation be approximated with  $\langle \cos \theta_i \rangle \approx -1$ , but it is not very accurate. For direct production, resulting pions travel in a wider range of angles, resulting in a wide spread of final energies. The spread means that the approximation with a  $\delta$ -function yielding a single value of  $\chi$  no longer is justified. A more precise description involves the probability distribution of the Mandelstam variable  $t$ ; the procedure is outlined in Appendix A in Hümmer et al. (2010) [8]. I have instead adapted their simplified model, that they outline in section 4.3. The approach is to approximate  $\chi$  by different constants depending on the energy  $\epsilon_r$ , and in that way make a step function that mimics the continuous function acquired using the more refined approach.

Returning to equation (3.17), one sees that for a constant  $\chi$ , that is  $\chi \neq \chi(\epsilon_r)$ , the  $\delta$ -function can instead be used to eliminate the integral over  $E$ . After some reshuffling in the  $\delta$ -function,  $Q_\pi$  instead takes the form

$$Q_\pi(E_\pi) = \int_{E_\pi}^{\infty} dE N_p(E) \cdot c \int_{\frac{\epsilon_{\text{th}} m_p}{2E}}^{\infty} d\varepsilon n_\gamma(\varepsilon) \times \sum_{\text{IT}} \frac{1}{2} \left( \frac{m_p}{E\varepsilon} \right)^2 \frac{M^{\text{IT}}}{\chi^{\text{IT}}} \int_{\epsilon_{\text{th}}}^{\frac{2E\varepsilon}{m_p}} d\epsilon_r \epsilon_r \sigma^{\text{IT}}(\epsilon_r) \delta\left(\frac{E_\pi}{\chi^{\text{IT}}} - E\right). \quad (3.42)$$

Evaluating the integral over  $E$  with the  $\delta$ -function, one obtains

$$Q_\pi(E_\pi) = N_p\left(\frac{E_\pi}{\chi^{\text{IT}}}\right) \cdot c \int_{\frac{\epsilon_{\text{th}} m_p \chi^{\text{IT}}}{2E_\pi}}^{\infty} d\varepsilon n_\gamma(\varepsilon) \times \sum_{\text{IT}} \frac{1}{2} \left( \frac{m_p \chi^{\text{IT}}}{\varepsilon E_\pi} \right)^2 \frac{M^{\text{IT}}}{\chi^{\text{IT}}} \int_{\epsilon_{\text{th}}}^{\frac{2\varepsilon E_\pi}{m_p \chi^{\text{IT}}}} d\epsilon_r \epsilon_r \sigma^{\text{IT}}(\epsilon_r), \quad (3.43)$$

as long as  $E_\pi/\chi^{\text{IT}}$  is within the proton energy integral limits.

The integral over  $\epsilon_r$  is tricky. It is approximated by a polynomial  $f^{\text{IT}}$  as

$$f^{\text{IT}}\left(\frac{2E\varepsilon}{m_p}\right) = \begin{cases} 0 & \frac{2E\varepsilon}{m_p} < \epsilon_{\text{min}}^{\text{IT}} \\ I^{\text{IT}}\left(\frac{2E\varepsilon}{m_p}\right) - I^{\text{IT}}(\epsilon_{\text{min}}^{\text{IT}}) & \epsilon_{\text{min}}^{\text{IT}} \leq \frac{2E\varepsilon}{m_p} < \epsilon_{\text{max}}^{\text{IT}} \\ I^{\text{IT}}(\epsilon_{\text{max}}^{\text{IT}}) - I^{\text{IT}}\left(\frac{2E\varepsilon}{m_p}\right) & \frac{2E\varepsilon}{m_p} \geq \epsilon_{\text{max}}^{\text{IT}}, \end{cases} \quad (3.44)$$

where, with  $x = \log_{10}\left(\frac{2E\varepsilon}{m_p} \frac{1}{\text{GeV}}\right)$

$$I^{\text{IT}}\left(\frac{2E\varepsilon}{m_p}\right) = \begin{cases} 0 & \frac{2E\varepsilon}{m_p} < 0.17 \text{ GeV} \\ 35.9533 + 84.0859x + 110.765x^2 + 102.728x^3 + 40.4699x^4 & 0.17 \text{ GeV} \leq \frac{2E\varepsilon}{m_p} < 0.96 \text{ GeV} \\ 30.2004 + 40.5478x + 2.03074x^2 - 0.387884x^3 + 0.025044x^4 & \frac{2E\varepsilon}{m_p} \geq 0.96 \text{ GeV}, \end{cases} \quad (3.45)$$

and

$$I^{\text{T2}} \left( \frac{2E\varepsilon}{m_p} \right) = \begin{cases} 0 & \frac{2E\varepsilon}{m_p} < 0.4 \text{ GeV} \\ -3.4083 + 16.2864 \frac{m_p}{2E\varepsilon} + \\ 40.7160 \ln \left( \frac{2E\varepsilon}{m_p} \right) & \frac{2E\varepsilon}{m_p} \geq 0.4 \text{ GeV}. \end{cases} \quad (3.46)$$

The direct production is split up into three different interactions for production channel T1: one for low values of  $\epsilon_r$ , one for intermediate values, and one for high values. T2 is split into four interactions: three for the first created pion and one for the second. The values of  $\epsilon_{\text{min}}^{\text{IT}}$  and  $\epsilon_{\text{max}}^{\text{IT}}$  needed to calculate  $f^{\text{IT}}$ , together with  $\chi^{\text{IT}}$ , and the multiplicities for the seven different interactions can all be found in table 5 in Hümmer et al. (2010) [8].

The contribution from direct production is then calculated as

$$Q_\pi(E_\pi) = N_p \left( \frac{E_\pi}{\chi^{\text{IT}}} \right) \cdot c \int_{\frac{\epsilon_{\text{th}} m_p \chi^{\text{IT}}}{2E_\pi}}^{\infty} d\varepsilon n_\gamma(\varepsilon) \times \sum_{\text{IT}} \frac{1}{2} \left( \frac{m_p \chi^{\text{IT}}}{\varepsilon E_\pi} \right)^2 \frac{M^{\text{IT}}}{\chi^{\text{IT}}} f^{\text{IT}} \left( \frac{2E\varepsilon}{m_p} \right). \quad (3.47)$$

### 3.10 Multipion production

The cross section for multipion production is given by summing the two following contributions

$$\sigma^{\text{Multi-1}}(\epsilon_r) = 80.3 \text{ Qf}(\epsilon_r, 0.5, 0.1) s^{-0.34}, \quad (3.48)$$

and

$$\sigma^{\text{Multi-2}}(\epsilon_r) = \begin{cases} 0 & \epsilon_r \leq 0.85 \\ [1 - \exp(-\frac{\epsilon_r - 0.85}{0.69})] \times (29.3 s^{-0.34} + 59.3 s^{0.095}) & \epsilon_r > 0.85, \end{cases} \quad (3.49)$$

where  $s$  is given in equation (3.22). The cross sections are given in  $\mu\text{barn}$  and  $\epsilon_r$  in GeV. The function Qf is given by [9]

$$\text{Qf}(\epsilon_r, \epsilon_{\text{th}}, w) = \begin{cases} 0 & \epsilon_r \leq \epsilon_{\text{th}} \\ \frac{\epsilon_r - \epsilon_{\text{th}}}{w} & \epsilon_{\text{th}} < \epsilon_r < \epsilon_{\text{th}} + w \\ 1 & \epsilon_r \geq \epsilon_{\text{th}} + w. \end{cases} \quad (3.50)$$

As can be seen in figure 3.2, the cross section for multipion production completely dominates for all energies above a few GeVs.

Similarly to the direct production channel, the approximation with a  $\delta$ -function for the resulting pion energies is not good enough and one is therefore left with equation (3.43). Once more, I will use a simplified model to approximate the  $\epsilon_r$  integral, this time following the technique described in section 4.4.2 in [8]. The multipion production channel is split into fourteen different interactions with different threshold energies  $\epsilon_{\text{min}}^{\text{IT}}$  and  $\epsilon_{\text{max}}^{\text{IT}}$ , different values for  $\chi^{\text{IT}}$  and  $M^{\text{IT}}$ , as well as different constant cross sections  $\sigma^{\text{IT}}$ . The reason for splitting it up into so many parts, is because the multiplicities  $M^{\text{IT}}$  change with  $\epsilon_r$ ; the more available energy, the more pions will be created in the QCD fragmentation. These will receive a smaller portion of the parent proton energy, so  $\chi$  will decrease with increasing  $\epsilon_r$ .

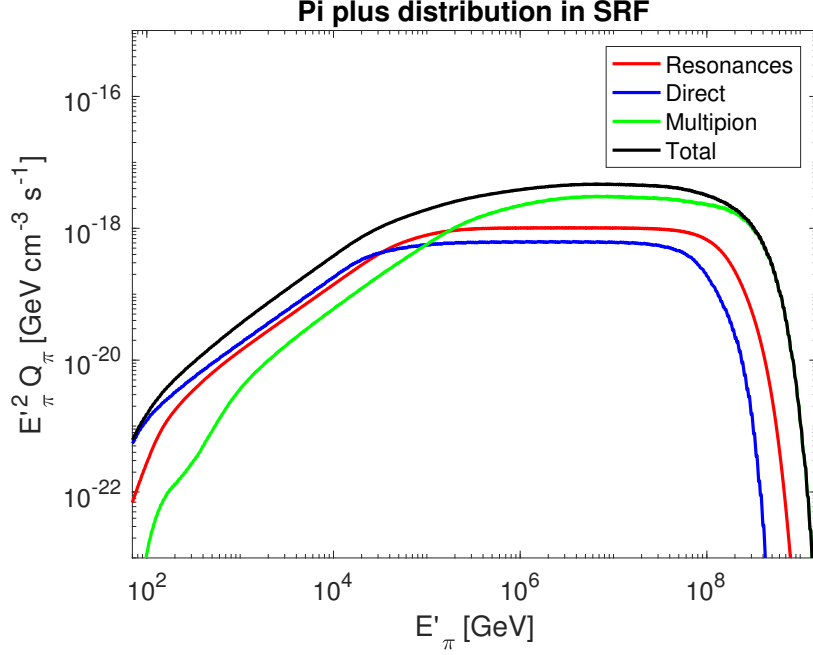


**Figure 3.3:** The different production channels contribution to the final  $\pi^+$ -distribution. It is clear that all channels are important to correctly predict the shape. Figure reproduced from Hümmer et al. (2010) [8].

The  $\epsilon_r$  integral is in this case replaced with the function

$$f^{\text{IT}}\left(\frac{2E\varepsilon}{m_p}\right) = \begin{cases} 0 & \frac{2E\varepsilon}{m_p} < \epsilon_{\text{min}}^{\text{IT}} \\ \sigma^{\text{IT}} \left[ \left(\frac{2E\varepsilon}{m_p}\right)^2 - \left(\epsilon_{\text{min}}^{\text{IT}}\right)^2 \right] & \epsilon_{\text{min}}^{\text{IT}} \leq \frac{2E\varepsilon}{m_p} < \epsilon_{\text{max}}^{\text{IT}} \\ \sigma^{\text{IT}} \left[ \left(\epsilon_{\text{max}}^{\text{IT}}\right)^2 - \left(\epsilon_{\text{min}}^{\text{IT}}\right)^2 \right] & \frac{2E\varepsilon}{m_p} \geq \epsilon_{\text{max}}^{\text{IT}}, \end{cases} \quad (3.51)$$

where all relevant quantities are given in table 6 in Hümmer et al. (2010) [8]. Inserting equation (3.51) into equation (3.47) yields the contribution from multipion production.

Figure 3.3 depicts the contributions from the different production channels to the resulting  $\pi^+$ -distribution. Proton and photon distributions are from the GRB benchmark in Hümmer et al. (2010), described in Appendix C in [8]. From the figure it is evident that all production channels contribute. At the lowest energies, the direct production channel dominates. Then there is a constant increase where direct production and resonance contributions are roughly equal, and for energies  $\epsilon_r \geq 5$  GeV multipion production dominates.

# Chapter 4

## Neutrino spectra

In this chapter, I will outline the procedure of obtaining the neutrino distribution from a known pion distribution. Section 4.1 explains the synchrotron cooling experienced by the charged pions and muons before their decay. Section 4.2 generates the neutrino distribution from the synchrotron cooled distributions and finally, section 4.3 deals with the phenomenon of neutrino oscillations and how it will effect the measurements. While the last chapter was general, this chapter is set in an astrophysical setting, where present magnetic fields and neutrino oscillations need to be taken into account.

### 4.1 Synchrotron cooling

The final neutrino distribution will be obtained by pion and muon decays as described in the decay chains in equations (2.5) and (2.6). However, the decayed particles will not have the same energy distribution as the initial particles, as they will have had time to cool through synchrotron cooling before their decay. Both charged pions and muons will be subjected to synchrotron cooling, and this section will derive an expression for the decay distribution  $N^{\text{dec}}$  as a function of the initial distribution  $N$ . The derivation will be general, and therefore valid for both particle species.

I will start by formulating the particle continuity equation. This equation has three terms: One term associated with synchrotron cooling of particles, one sink term associated with decay, and one term associated with particles escaping the shell. I assume that the magnetic field is only present in the shell, and so particles will not experience cooling once they escape the shell. The continuity equation is

$$\frac{\partial N(E, t)}{\partial t} = \frac{\partial}{\partial E} \left[ N(E, t) \left( \frac{dE}{dt} \right)^{\text{sync}} \right] - \frac{N(E, t)}{\gamma\tau_0} - \frac{N(E, t)}{t_{\text{esc}}}, \quad (4.1)$$

which should be solved for  $N(E, t)$ . This can be done using the method of characteristics. Introduce a common variable  $s$ , and rewrite  $N(E(s), t(s))$ . Using the chain rule, one obtains

$$\frac{\partial N}{\partial s} = \frac{\partial N}{\partial E} \frac{dE}{ds} + \frac{\partial N}{\partial t} \frac{dt}{ds}, \quad (4.2)$$

which becomes

$$-\frac{\partial N}{\partial s} + \frac{\partial N}{\partial E} \frac{dE}{ds} + \frac{\partial N}{\partial t} \frac{dt}{ds} = 0. \quad (4.3)$$

By rewriting equation (4.1) in a similar fashion

$$\frac{\partial N}{\partial t} - \frac{\partial}{\partial E} \left[ N \left( \frac{dE}{dt} \right)^{\text{sync}} \right] + \frac{N}{\gamma\tau_0} + \frac{N}{t_{\text{esc}}} = 0, \quad (4.4)$$

one can directly compare coefficients between equations (4.3) and (4.4) to determine

$$\frac{dt}{ds} = 1 \quad (4.5a)$$

$$\frac{dE}{ds} = - \left( \frac{dE}{dt} \right)^{\text{sync}} \quad (4.5b)$$

$$\frac{\partial N}{\partial s} = N \frac{\partial}{\partial E} \left( \frac{dE}{dt} \right)^{\text{sync}} - \frac{N}{\gamma\tau_0} - \frac{N}{t_{\text{esc}}}. \quad (4.5c)$$

The first is trivially solved as

$$t = s. \quad (4.6)$$

For an isotropic distribution of charged particles, synchrotron cooling is given by

$$\left( \frac{dE}{dt} \right)^{\text{sync}} = -\frac{4}{3} \sigma_{\gamma,P} c \beta^2 \gamma^2 U_B, \quad (4.7)$$

where  $\sigma_{\gamma,P}$  is the cross section for scattering of a parent particle with a photon, and  $U_B$  is the magnetic energy density. Rewriting  $\gamma = E/(mc^2)$ , equation (4.7) becomes

$$\left( \frac{dE}{dt} \right)^{\text{sync}} = -\alpha E^2 \quad (4.8)$$

where  $\alpha = \frac{4}{3} \frac{\sigma_{\gamma,P} \beta^2 U_B}{m^2 c^3}$ . Equation (4.5b) can now be solved. Separation of variables yields

$$\frac{dE}{E^2} = \alpha ds. \quad (4.9)$$

Integrating and solving for  $E$  gives

$$E = \frac{1}{\frac{1}{E_0} + \alpha s} \quad (4.10)$$

where  $E_0$  is initial energy. Moving on to equation (4.5c), one gets

$$\begin{aligned} \frac{\partial N}{\partial s} = N \frac{\partial}{\partial E} (-\alpha E^2) - \frac{Nmc^2}{E\tau_0} - \frac{N}{t_{\text{esc}}} = \\ - \left[ \frac{2\alpha N}{\frac{1}{E_0} + \alpha s} + \frac{Nmc^2}{\tau_0} \left( \frac{1}{E_0} + \alpha s \right) + \frac{N}{t_{\text{esc}}} \right]. \end{aligned} \quad (4.11)$$

Separating variables once again and integrating gives

$$\ln(N) = -2 \ln \left( \frac{1}{E_0} + \alpha s \right) - \frac{mc^2}{\tau_0} \left( \frac{s}{E_0} + \frac{\alpha s^2}{2} \right) - \frac{s}{t_{\text{esc}}} + \tilde{C}, \quad (4.12)$$

where  $\tilde{C}$  is an integration constant. After recalling that  $s = t$ , this can be solved as

$$N = C \left( \frac{1}{E_0} + \alpha t \right)^{-2} \exp \left( -\frac{mc^2}{\tau_0} \left( \frac{t}{E_0} + \frac{\alpha t^2}{2} \right) - \frac{t}{t_{\text{esc}}} \right), \quad (4.13)$$

where  $C = \exp \tilde{C}$ . Requiring  $N = N_0$  for  $t = 0$ , one finds  $C = N_0/E_0^2$ . Finally, the particle decay distribution  $N^{\text{dec}}$  is given by time integrating the sink term and the escape term:

$$N^{\text{dec}}(E, t) = \int_0^\infty \left[ \frac{N(E, t)mc^2}{E\tau_0} + \frac{N(E, t)}{t_{\text{esc}}} \right] dt. \quad (4.14)$$

The minus signs do not appear in the equation above, as the decay and escape terms are not sink terms, but source terms for  $N^{\text{dec}}$ .

The scattering cross section is defined as

$$\sigma_{\gamma, P} = \frac{8\pi}{3} \frac{q_P^4}{m_P^2 c^4}, \quad (4.15)$$

where  $q_P$  is the parent particle charge. When  $|q_P| = |q_e|$  as it is for parent pions and muons, the only thing that differs between  $\sigma_{\gamma, P}$  and the ordinary Thomson cross section for electron-photon scattering  $\sigma_T$ , is the mass. Thus, the cross section can be expressed as

$$\sigma_{\gamma, P} = \frac{m_e^2}{m_P^2} \sigma_T, \quad (4.16)$$

and with  $\sigma_T = 6.6525 \cdot 10^{-25} \text{ cm}^2$  [12],  $\sigma_{\gamma, P}$  can easily be determined for both pions and muons.

The effect of synchrotron cooling on the  $\pi^+$  distribution previously shown in figure 3.3, can be seen in figure 4.1. In the figure, the decay distribution  $N_{\pi^+}^{\text{dec}}$  is shown with thicker lines and the distribution before cooling  $N_{\pi^+}$  is shown for comparison with thinner lines. It is evident that the higher energy spectrum is much more effected than the lower energy spectrum, this is of course due to synchrotron cooling being proportional to  $E^2$  (see equation (4.8)).

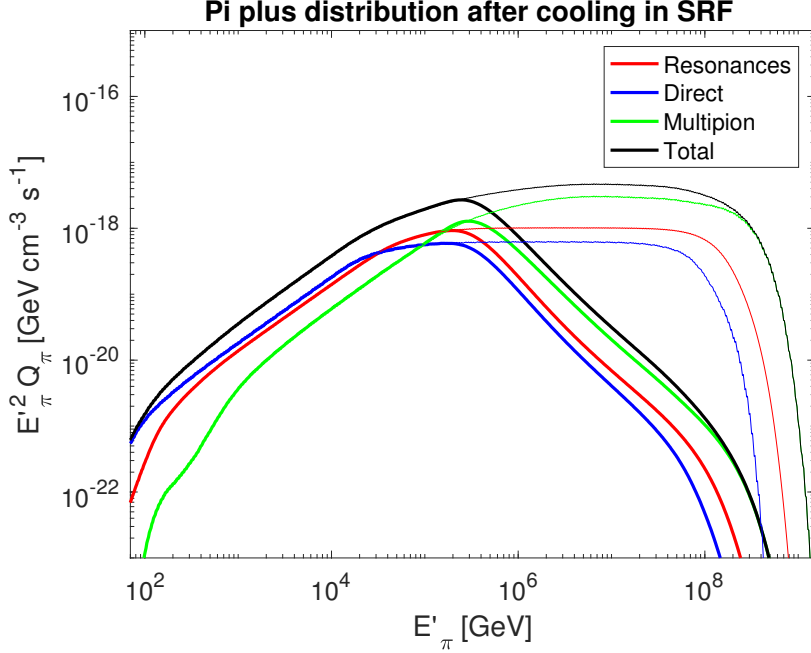


**Figure 4.1:** The effect of synchrotron cooling. The thin lines depict the initial distribution  $N_{\pi^+}$  and the thick lines show the particle decay distribution  $N_{\pi^+}^{\text{dec}}$ . The figure was obtained with a magnetic field energy density  $U_B = 10^{12} \text{ GeV cm}^{-3}$  and  $t_{\text{esc}} = \Gamma l/c = 0.5 \text{ s}$ .

## 4.2 Neutrino distribution

The resulting neutrino spectra from the pion, and subsequently muon decays, are calculated as in section 4 in Lipari et al. (2007) [13]. The distribution of daughter particle  $b$  obtained through the decay of parent particle  $a$  is

$$N_b(E_b) = \int_{E_b}^{\infty} dE_a N_a^{\text{dec}}(E_a) \frac{dn_{E_a \rightarrow E_b}}{dE_b} \quad (4.17)$$

where  $N_a^{\text{dec}}$  is obtained through the method outlined in the previous section. There is no time dependence, as  $N_a^{\text{dec}}$  already is time integrated. The equation above can be applied to both cooled  $\pi^{\pm}$  and  $\mu^{\pm}$ . The term  $dn_{E_a \rightarrow E_b}/dE_b$  tells you what energies  $E_b$  the daughter particle can receive from parent particle energy  $E_a$ , and looking back at equation (3.16), I rewrite this term as

$$\frac{dn_{E_a \rightarrow E_b}}{dE_b}(E_a, E_b) = \frac{1}{E_a} F_{E_a \rightarrow E_b} \left( \frac{E_b}{E_a} \right), \quad (4.18)$$

where  $F_{E_a \rightarrow E_b}$  is a scaling function. For  $\pi^{\pm}$ , this is a two body decay problem and the neutrino energy scaling function is quite easily determined as

$$F_{E_{\pi^+ \rightarrow E_{\nu\mu}}}(x) = F_{E_{\pi^- \rightarrow E_{\bar{\nu}\mu}}}(x) = \frac{1}{1 - r_{\pi}} \Theta(1 - r_{\pi} - x), \quad (4.19)$$

where  $\Theta(x)$  is the Heaviside step function and  $r_{\pi} = m_{\mu}^2/m_{\pi}^2$ .

In the scaling function for muons, it is necessary to account for the helicity of the created muons, because the second decay is helicity dependent. Whether the muon is

left- or right-handed will affect the final flavor ratios. The scaling functions are

$$F_{E_{\pi^+} \rightarrow E_{\mu_R^+}}(x) = F_{E_{\pi^-} \rightarrow E_{\mu_L^-}}(x) = \frac{r_\pi(1-x)}{x(1-r_\pi)^2} \Theta(x-r_\pi) \quad (4.20)$$

$$F_{E_{\pi^+} \rightarrow E_{\mu_L^+}}(x) = F_{E_{\pi^-} \rightarrow E_{\mu_R^-}}(x) = \frac{x-r_\pi}{x(1-r_\pi)^2} \Theta(x-r_\pi).$$

The scaling functions for the neutrinos created in the second decay are

$$F_{E_{\mu^+} \rightarrow E_{\bar{\nu}_\mu}}(x, h) = F_{E_{\mu^-} \rightarrow E_{\nu_\mu}}(x, -h) = \left( \frac{5}{3} - 3x^2 \frac{4x^3}{3} \right) + h \left( -\frac{1}{3} + 3x^2 - \frac{8x^3}{3} \right) \quad (4.21)$$

$$F_{E_{\mu^+} \rightarrow E_{\nu_e}}(x, h) = F_{E_{\mu^-} \rightarrow E_{\bar{\nu}_e}}(x, -h) = (2 - 6x^2 + 4x^3) + h(2 - 12x + 18x^2 - 8x^3),$$

where  $h$  accounts for the helicity:  $h = 1$  for right-handed muons and  $h = -1$  for left-handed ones. Inserting these into equation (4.17), together with the synchrotron cooled decay distributions of muons  $N_\mu^{\text{dec}}$ , gives the distribution of neutrinos created in the second decay. Summing up the neutrinos produced in the pion decay and the subsequent muon decay gives the total neutrino production.

### 4.3 Neutrino oscillations

The phenomenon that a neutrino originally created as one flavor, has a non-zero probability of being detected as another flavor after propagation, is called neutrino oscillation. Neutrino oscillation arises because there is mass difference between the neutrinos. A neutrino of flavor  $\alpha$  can be written as a superposition of mass states as

$$|\nu_\alpha\rangle = \sum_i U_{\alpha i} |\nu_i\rangle \quad (4.22)$$

where  $U_{\alpha i}$  is a unitary matrix and  $|\nu_i\rangle$  are the different mass eigenstates. In the case of three neutrino flavors and three mass eigenstates, this becomes

$$\begin{bmatrix} |\nu_e\rangle \\ |\nu_\mu\rangle \\ |\nu_\tau\rangle \end{bmatrix} = \begin{bmatrix} U_{e1} & U_{e2} & U_{e3} \\ U_{\mu1} & U_{\mu2} & U_{\mu3} \\ U_{\tau1} & U_{\tau2} & U_{\tau3} \end{bmatrix} \begin{bmatrix} |\nu_1\rangle \\ |\nu_2\rangle \\ |\nu_3\rangle \end{bmatrix}.$$

The probability that a neutrino of flavor  $\alpha$  will be detected as a neutrino with flavor  $\beta$  is, in the three flavor case, given by

$$P_{\alpha \rightarrow \beta} = \delta^{\alpha\beta} - 4 \sum_{k>j} \text{Re}(U_{\alpha,k}^* U_{\beta,k} U_{\alpha,j} U_{\beta,j}^*) \sin^2 \left( \frac{\Delta m_{kj}^2 L}{4E} \right) + 2 \sum_{k>j} \text{Im}(U_{\alpha,k}^* U_{\beta,k} U_{\alpha,j} U_{\beta,j}^*) \sin^2 \left( \frac{\Delta m_{kj}^2 L}{2E} \right), \quad (4.23)$$

where  $U_{\alpha,k}$  refers to the  $\{\alpha, k\}$  element of the  $U$  matrix given above,  $\Delta m_{kj}$  is the mass difference between mass state  $k$  and  $j$ ,  $L$  is the length the neutrino has propagated and  $E$  is the neutrino energy [14, 15].

In the assumption where one mass difference is much greater than the other, say  $\Delta m_{12}^2 \ll \Delta m_{13}^2$ , the expression simplifies significantly, and the flavor changing probability can be written

$$P_{\alpha \rightarrow \beta} = \sin^2(2\theta_{12}) \sin^2\left(\frac{\Delta m_{kj}^2 L}{4E}\right). \quad (4.24)$$

This is called quasi-two neutrino oscillations, as the expression is the same as if there had only been two neutrino flavors [14]. As the GRBs distance to earth is arbitrary, and the final result will be an all sky flux, the second argument is equally likely to take any multiple value in the  $[0, 2\pi]$  range. I therefore take the average of the second sin-factor, which for  $\sin^2(x)$  is simply  $1/2$ . With

$$\sin^2 \theta_{12} = 0.31,$$

at  $1\sigma$  confidence level [16], one gets

$$\sin^2(2\theta) = 0.85. \quad (4.25)$$

The detectable distribution of muon neutrinos, accounting for neutrino oscillations is therefore

$$N_{\nu_\mu}^{\text{det}} = \left(1 - \frac{1}{2} \sin^2(2\theta)\right) N_{\nu_\mu} + \left(\frac{1}{2} \sin^2(2\theta)\right) N_{\nu_e} = \quad (4.26)$$

$$0.575 N_{\nu_\mu} + 0.425 N_{\nu_e}$$

where  $N_{\nu_\mu}$  and  $N_{\nu_e}$  are the original muonic and electronic neutrino distributions respectively. By interchanging  $N_{\nu_\mu}$  with  $N_{\nu_e}$  in the equation above, one gets the expression for  $N_{\nu_e}^{\text{det}}$ .

# Chapter 5

## Simulation outline

The simulation has been done following a paper by Bustamante et al. (2016) [17]. The main difference is that they used a Monte Carlo simulation program called NeuCosma [18], while I have calculated the secondary particle distributions as outlined in the previous chapter. The simulation is done in 1D using the multi-shell internal shock model. The user can give several inputs to the simulation: The number of shells emitted, distribution of shell bulk Lorentz factors, distance between each shell and the width of the shells, total observed gamma radiation etc. The simulation consists of three major parts: Burst setup, burst evolution, and observation.

### 5.1 Burst setup

Before the simulation can start, all the parameters of the burst must be set. After the setup, there will be  $N_{\text{shells}}$  shells, all of which has the set of parameters  $\{\Gamma_{k,0}, m_{k,0}, l_{k,0}, r_{k,0}\}$ : subscript  $k, 0$  here indicates the  $k$ -th shell and initial values.  $\Gamma_{k,0}$  is the initial bulk Lorentz factor,  $m_{k,0}$  is its mass,  $l_{k,0}$  its width, and  $r_{k,0}$  is its (rear) radius to the central engine (i.e. front radius is given by  $r_{k,0} + l_{k,0}$ ). In this thesis, I will study five different benchmark GRBs. The benchmarks differ in the setup, and how the initial parameters are set will be described presently.

#### 5.1.1 Initial Lorentz factors

The bulk Lorentz factor for each shell are randomized from a lognormal distribution

$$\ln \left( \frac{\Gamma_{k,0} - 1}{\Gamma_0^k - 1} \right) = \sigma^{\text{logn},k} x, \quad (5.1)$$

where  $x$  is a random variable from a normal (Gaussian) distribution with mean  $\mu^{\text{norm}} = 0$  and standard deviation  $\sigma^{\text{norm}} = 1$ . This gives

$$\Gamma_{k,0} = (\Gamma_0^k - 1) e^{\sigma^{\text{logn},k} x} + 1 = (\Gamma_0 - 1)y + 1. \quad (5.2)$$

The simulation then uses MATLAB function *lognrnd* to generate  $N_{\text{shells}}$  values  $y$ , that are lognormal random values with mean  $\mu^{\text{logn}} = 0$  and standard deviation  $\sigma^{\text{logn},k}$ .

In GRB 1,  $\Gamma_0^k$  and  $\sigma^{\text{logn},k}$  are both constant and the same for all  $k$ , and they are input parameters chosen by the user. In all other benchmarks, they will oscillate between two

set values  $\Gamma_{0,1}$  and  $\Gamma_{0,2}$ , and  $\sigma_{0,1}^{\text{logn}}$  and  $\sigma_{0,2}^{\text{logn}}$ . This can represent various different central engine behaviors such as decreasing activity, increasing activity, varying emittance power from a varying mass emittance to name a few scenarios. In these cases,  $\Gamma_0^k$  and  $\sigma^{\text{logn},k}$  are given by

$$\begin{aligned}\Gamma_0^k &= (\Gamma_{0,2} - \Gamma_{0,1}) \times \sin^2 \left( \frac{k}{N_{\text{shells}}} N_{\text{osc}} \cdot \frac{\pi}{2} \right) + \Gamma_{0,2}, \\ \sigma^{\text{logn},k} &= (\sigma_{0,2}^{\text{logn}} - \sigma_{0,1}^{\text{logn}}) \times \sin^2 \left( \frac{k}{N_{\text{shells}}} N_{\text{osc}} \cdot \frac{\pi}{2} \right) + \sigma_{0,2}^{\text{logn}}.\end{aligned}\tag{5.3}$$

Here,  $N_{\text{osc}}$  is the number of oscillations between  $\Gamma_{0,1}$  and  $\Gamma_{0,2}$ , specifically  $N_{\text{osc}} = 2$  means first an increase/decrease from  $\Gamma_{0,1}$  to  $\Gamma_{0,2}$  and then back again to  $\Gamma_{0,1}$ . The calculated  $\Gamma_0^k$  and  $\sigma^{\text{logn},k}$  are then plugged into equation (5.1) to get  $\Gamma_{k,0}$ . A figure of the initial  $\Gamma$  distributions for GRB benchmarks 1-5 is shown in figure 5.1. The input parameters of the benchmarks are given in table 5.1.

### 5.1.2 Initial masses

The masses of the shells are given from the relation  $E_{\text{kin}}^{\text{iso}} = (\Gamma_{k,0} - 1)m_{k,0}c^2 \approx \Gamma_{k,0} m_{k,0}c^2$ .  $E_{\text{kin}}^{\text{iso}}$  is an input variable, common to all shells. Thus, the mass for the  $k$ -th shell is

$$m_{k,0} = \frac{E_{\text{kin}}^{\text{iso}}}{\Gamma_{k,0}c^2}.\tag{5.4}$$

The interpretation for this is that all shells are given the same amount of kinetic energy but a varying mass, and this varying mass yields the different Lorentz factors. The input variable  $E_{\text{kin}}^{\text{iso}}$  is directly proportional to the total emitted energy and will therefore only scales the output energies up or down. By later scaling the energy to a set total radiated gamma energy  $E_{\gamma,\text{set}}^{\text{iso}}$ , the choice of  $E_{\text{kin}}^{\text{iso}}$  will become irrelevant, see Appendix A for details.

### 5.1.3 Initial widths and shell distances

The widths of the shells  $l_{k,0}$  are set to be constant. More specifically, they are given as the emission time  $\delta t$  times  $c$ :

$$l_{k,0} = \delta t c,\tag{5.5}$$

for all  $k$ . The emission time is chosen similar to the variability time observed at Earth,  $\delta t \sim t_v \approx 0.01$  s. The rest time in between emitting two shells is assumed to be the same as the ejection time of a shell, and so if the distance between shell  $k$  and shell  $k + 1$  is called  $d_k$ , then  $d_k = 0.01 c$ , just as  $l_k$ .

### 5.1.4 Initial radii

The radii for the initial shells can easily be calculated as

$$r_{k,0} = r_{\text{inner}} + (N_{\text{shells}} - k)(l_0 + d_0),\tag{5.6}$$

where  $r_{\text{inner}}$  is the radius of the innermost shell, set by the user. I have set this value to  $r_{\text{inner}} = 10^8$  cm, similar to Bustamante et al. (2016) [17]. The number of shells are given such that  $k = 1$  represents the shell emitted first. It is therefore the shell furthest away from the central engine, and the higher the  $k$  value, the closer to the central engine.

**Table 5.1:** GRB benchmark parameter inputs

GRB	$\Gamma_{0,1}$	$\Gamma_{0,2}$	$\sigma_{0,1}^{\text{logn}}$	$\sigma_{0,2}^{\text{logn}}$	$N_{\text{osc}}$	$E_{\gamma,\text{set}}^{\text{iso}}$
1	500	-	1	-	-	$10^{53}$
2	500	50	1	0.1	1	$10^{53}$
3	50	500	0.1	0.1	2	$10^{52}$
4	50	500	0.1	1	10	$10^{53}$
5	50	500	0.1	0.1	10	$10^{53}$

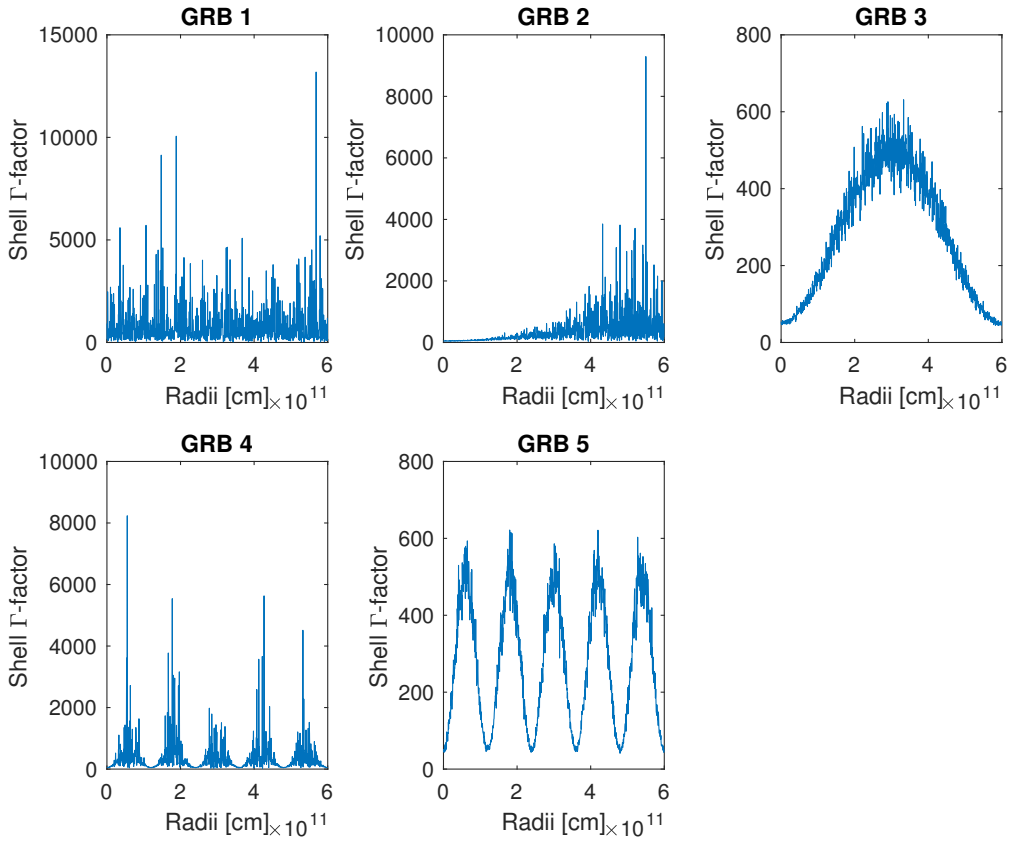


**Figure 5.1:** Initial  $\Gamma$ -distribution as a function of  $r$  in cm for the five different benchmark GRBs. The central engine is situated at  $r = 0$ .

## 5.2 Burst evolution

After the burst setup, there are  $N_{\text{shells}}$  shells distributed equidistantly with the innermost shell at  $r = r_{\text{inner}}$  for  $k = N_{\text{shells}}$ , and the radii between two neighboring shells differing by  $l_0 + d_0$ . The bulk Lorentz factors of the shells are randomly distributed around set values  $\Gamma_{0,1}$  and  $\Gamma_{0,2}$  and have predetermined deviations  $\sigma_{0,1}^{\text{logn}}$  and  $\sigma_{0,2}^{\text{logn}}$ . The  $\Gamma$  then determines the initial masses through  $m_{k,0} = E_{\text{kin}}^{\text{iso}}/\Gamma_{k,0}$ . Once this setup is done, the simulation can start.

The run follows the algorithm described in the following four steps:

1. Calculate the time until the next collision  $\Delta t_{\text{next}}$ , and for what pair of shells this will occur.
2. Propagate all non-interacting shells to their new positions  $r_{k,\text{new}} = r_{k,\text{previous}} + v_k \Delta t_{\text{next}}$  where  $v_k$  is the speed of shell  $k$ .
3. Calculate the total energy radiated in the collision  $E_{\text{coll}}^{\text{iso}}$  and remove the two colliding shells. Create a new merged shell with the parameter set  $\{\Gamma_m, m_m, l_m, r_m\}$  at the collision radius.
4. If at this stage, any of the following is true, the simulation ends:
  - All shells have propagated beyond  $r_{\text{cbm}}$ , the radius of the circumburst medium.
  - All shells have ascending values of  $\Gamma$ , so that no shell can catch up with the shell in front.
  - Only one shell remains.

If not, it returns to step 1.

Below follows a description of the procedure in each step.

**Step 1.** Calculating the time until the next collision and for which pair this occurs is straightforward. The time until a collision would occur between shell  $k$  and  $k + 1$  is

$$\Delta t_{k,k+1} = \frac{d_{k,k+1}}{v_{k+1} - v_k}. \quad (5.7)$$

The distance  $d_{k,k+1}$  is between the front radius of shell  $k + 1$  and the rear radius of shell  $k$  is given by  $d_{k,k+1} = r_k - (r_{k+1} + l_{k+1})$ . If  $v_k > v_{k+1}$ , then  $\Delta t_{k,k+1}$  becomes negative and is discarded. This represents the front shell being faster than the rear shell, and in such a situation, a collision can never occur. When  $\Delta t_{k,k+1}$  is calculated for all shell pairs,  $\Delta t_{\text{next}}$  is set as the minimum of all valid  $\Delta t_{k,k+1}$ . The time for collision  $i$  is saved in a vector as  $t_{\text{coll},i} = t_{\text{coll},i-1} + \Delta t_{\text{next}}$ .

**Step 2.** In step 2, all shells are propagated using  $\Delta t_{\text{next}}$  calculated in step 1. The new positions for all shells are given by

$$r_{k,i} = r_{k,i-1} + v_k \Delta t_{\text{next}}, \quad (5.8)$$

where  $r_{k,i}$  is the position of shell  $k$  just as collision  $i$  occurs.

**Step 3.** The energy radiated in a collision is the difference in energy between the two parent shells and the resulting merged shell. In collision  $i$  between a fast shell  $k + 1$  and a slower shell  $k$ , the energy is

$$E_{\text{coll},i}^{\text{iso,u}} = (\Gamma_{k+1}m_{k+1}c^2 + \Gamma_k m_k c^2) - \Gamma_m m_m c^2, \quad (5.9)$$

where the superscript indicates that the energy release is isotropic in the progenitor source frame (spherical symmetry in the burst). The superscript u indicates that the energies are unscaled. The emitted energies will later be scaled to match a total observed  $\gamma$ -ray energy  $E_{\gamma,\text{set}}^{\text{iso}}$ , as described in subsection 5.4.2. The parameter set for the merged shell is calculated as in Bustamante et al. (2016) [17]. The bulk Lorentz factor for the merged shell  $\Gamma_m$  is calculated as

$$\Gamma_m = \sqrt{\frac{m_{k+1}\Gamma_{k+1} + m_k\Gamma_k}{m_{k+1}/\Gamma_{k+1} + m_k/\Gamma_k}}. \quad (5.10)$$

The mass is trivially given as the sum of the masses of the parent shells

$$m_m = m_{k+1} + m_k. \quad (5.11)$$

The width  $l_m$  is more tricky. It was derived by Kobayashi et al. (1997) [6] to be

$$l_m = l_k \frac{\beta_{\text{fs}} - \beta_m}{\beta_{\text{fs}} - \beta_k} + l_{k+1} \frac{\beta_m - \beta_{\text{rs}}}{\beta_{k+1} - \beta_{\text{rs}}}, \quad (5.12)$$

where  $\beta_{\text{fs(rs)}}$  is the  $\beta$ -factor of the forward (reverse) shock:  $\beta_{\text{fs(rs)}} = \sqrt{1 - \Gamma_{\text{fs(rs)}}^{-2}}$ . The forward and reverse shocks are the fronts that are created in the merger between the two shells, as the front of the faster shell propagates through the slower one, and the rear of the slower shell is traveling towards the rear of the faster one, see figure 10 in [17] for an illustration. The Lorentz factor  $\Gamma_{\text{fs(rs)}}$  is given by

$$\Gamma_{\text{fs(rs)}} = \Gamma_m \sqrt{\frac{1 + 2\Gamma_m/\Gamma_{k(k+1)}}{2 + \Gamma_m/\Gamma_{k(k+1)}}}. \quad (5.13)$$

The radius of the new merged shell is placed at the radius of its slower parent, i.e.,  $r_m = r_k$ , of course after the propagation of  $r_k$ , and the collision radii is recorded just as the collision time.

With all of its quantities updated, the merged shell is left in the simulation with the possibility to collide again.

**Step 4.** In step four, the simulation checks whether it should terminate or not. First, it checks whether all shells are beyond the radius of the circumburst medium where the shells starts decelerating. This is assumed to occur at  $r_{\text{cbm}} = 5.5 \times 10^{16}$  cm. All collision occurring further out than this are discarded in this simulation. If only some of the shells have reached this distance, then those shells are removed but the simulation still continues with the remaining ones. Secondly, it checks if all values of  $\Gamma_k$  are in ascending order. If this is so, no more collisions can happen and the simulation ends. Lastly, if there is only one shell remaining, the simulation ends as well.

If none of the criteria above is met, the simulation returns to step 1 and the procedure is repeated.

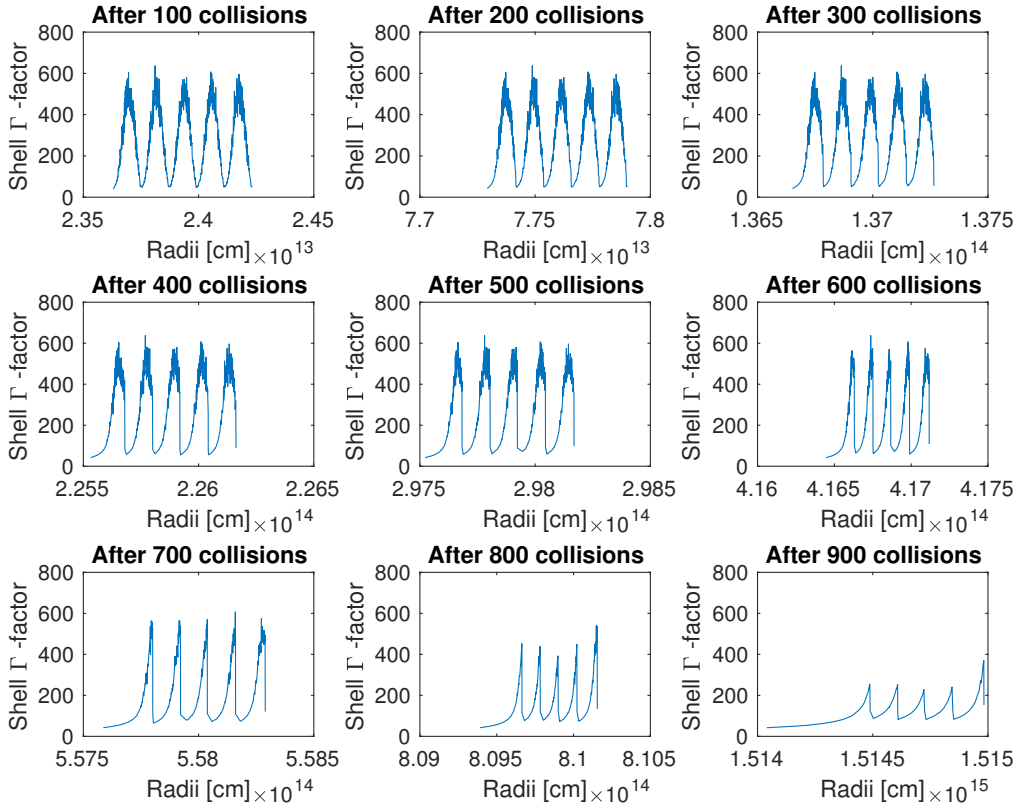


**Figure 5.2:** Shell Lorentz factor  $\Gamma$  as a function of radii during the burst evolution of GRB 5. By the end of the burst, all five pulses have smooth, sawtooth shapes with lower average value than originally.

### 5.3 Control of the code

It is very important to control that the code behaves as predicted. This can be done by seeing how values of different quantities behave during the burst. It is also interesting to see how properties evolve during the burst.

How the shell Lorentz factor  $\Gamma$  change during the burst evolution for GRB 5 can be seen in figure 5.2. As the burst progresses, each of the five pulses in the burst tends more and more to a smooth curve, with its highest value of  $\Gamma$  in front of the pulse. All initial ruggedness disappears as the fastest shells catch up with their slower companions. An overall decrease in  $\Gamma$  at the end of the burst compared to initial values is also visible.

Figure 5.3 depicts how some average values change during the burst evolution of GRB 4. Light blue line depicts average mass over initial average mass  $\langle m \rangle / \langle m_0 \rangle$ , the red line is the ratio  $\text{RMS}(\Gamma) / \text{RMS}(\Gamma_0)$  where RMS stands for root mean square, the yellow line shows the fraction of shells remaining, and the average velocity  $\langle \beta \rangle$  is shown in purple. Each dot represent a collision and the energy emitted in that collision compared to the average  $E_{\text{coll},i}^{\text{iso}} / \langle E \rangle$ , where  $E$  is the total energy emitted in the burst, including subphotospheric collisions. Whether a collision was below or above the photosphere is marked as well.

That the mass ratio increases is no surprise. In each shell collision, the merged shell's

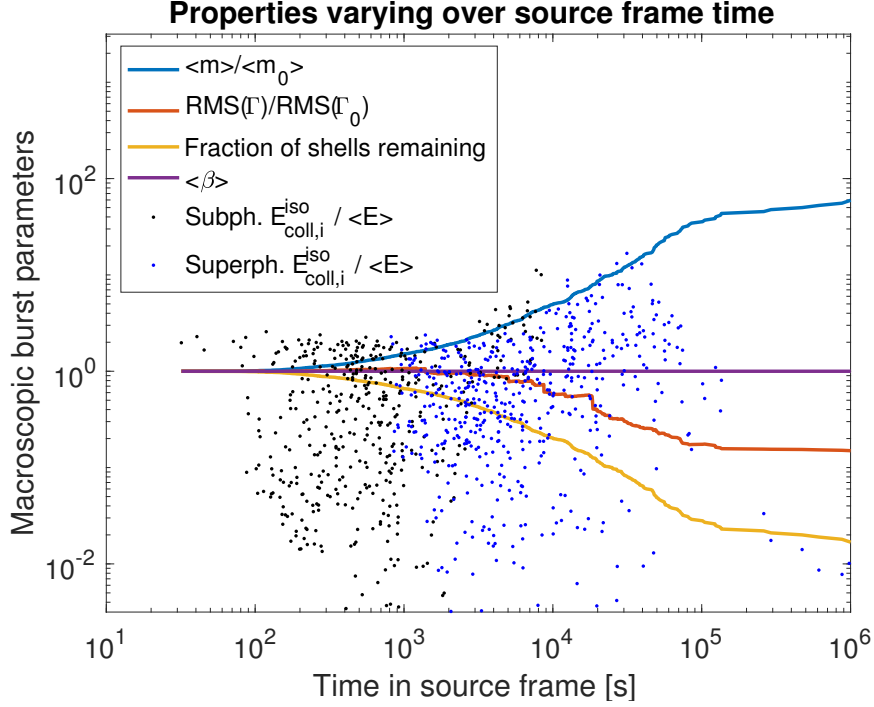


**Figure 5.3:** Burst evolution of quantities for GRB 4. The average mass increases, while the average  $\Gamma$  decreases. The average shell speed is  $\approx c$  throughout the burst. Collisions radii is relatively evenly spread out, with a tendency to higher energy collisions towards the end. Partial figure inspiration taken from Bustamante et al. (2016) [17].

mass is simply given as the sum of the two colliding shells masses, so naturally the mass fraction rises as the number of shells left decreases. It is interesting to see how unaffected the speed is, even though a large amount of energy is emitted. In the burst shown, there were 985 collisions, and the average  $\beta$  value after the last collision was  $\langle \beta \rangle = 0.99991$ . The average  $\Gamma$  decreases during the burst. This is of course in direct correlation to a decrease in  $\beta$ , even though that is not visible. The average  $\Gamma$  decrease is expected, because it is the shells kinetic energy that is transformed into radiation, as no mass-energy conversion is assumed. From the figure one can also see that the most energetic collisions happen at a rather late time. This is due to the periodic outflow of GRB 4. These collision are between the highest  $\Gamma$  of the pulse peaks with the lowest  $\Gamma$  of the pulse valleys. The reason why they occur at such late time, is because it is not until then they have had enough time to catch up; even the less energetic shells have  $\beta \approx 1$ .

## 5.4 Observation

After the burst evolution is done, one has to interpret all the data. In this section, I will describe how the saved data from the burst evolution leads to qualitative predictions.

### 5.4.1 Observation time

From the burst evolution, I have saved the time for each collision in a vector

$$t_{\text{coll}} = [t_{\text{coll},1}, t_{\text{coll},2}, \dots, t_{\text{coll},i}, \dots, t_{\text{coll},N_{\text{coll}}}], \quad (5.14)$$

where  $N_{\text{coll}}$  is the total number of shell collisions in the burst ( $N_{\text{coll}} \lesssim N_{\text{shells}}$ ) and  $t = 0$  at the start of the simulation. Similarly, I have saved all collision radii in the vector  $r_{\text{coll}}$ . The time until we on Earth observe radiation from a collision, is then given by the time it takes the radiation to travel to Earth plus the time that has already elapsed from the burst start until the collision occurs. If the distance from the central emitter to earth is  $D(z)$  for redshift  $z$ , then the observer time from the simulation start  $\tilde{t}_{\text{obs}}$  is given by

$$\tilde{t}_{\text{obs}} = (1 + z) \left( \frac{D(z) - r_{\text{coll}}}{c} + t_{\text{coll}} \right). \quad (5.15)$$

Two comments on this:

1. The term  $(1 + z)(D(z)/c)$  is only a dummy variable. What is of interest is the observer time from the moment light reaches us  $t_{\text{obs}}$ , and not from the simulation start. The term  $(1 + z)(D(z)/c)$  is a constant that is removed from all terms when the observation time is defined as  $t_{\text{obs}} = \tilde{t}_{\text{obs}} - \min[\tilde{t}_{\text{obs}}]$ .
2. Even though the burst duration in the simulation stretches over weeks, the total observed radiation will arrive within  $\sim 80$  seconds. This is because of the shells' velocities are so extremely close to  $c$ , that the emitted radiation from a collision hardly travels any faster than the shells themselves. Therefore, the observer time span depends more on the radial extension of the burst rather than when collisions occur. This can be seen from figure 5.4, showing each collision's energy as a fraction of the total, as a function of observer time. The shapes are similar to the initial  $\Gamma$ -distributions shown in figure 5.1.

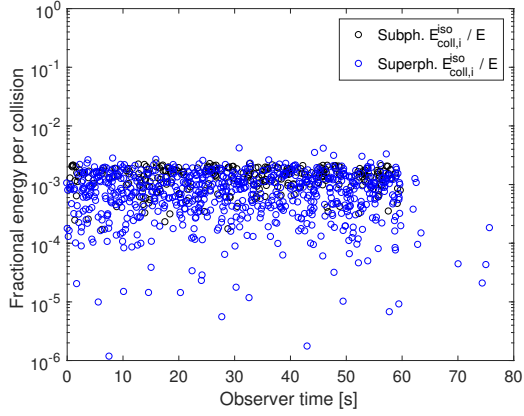
## 5.4.2 Energy output normalization

From the burst evolution, the energy emitted in each collision  $E_{\text{coll},i}^{\text{iso}}$  is calculated as in equation (5.9). This energy becomes internal energy in the merged shell, which is assumed to cool instantly and radiate this energy as secondary particles. How the energy is split, is an input parameter. Using the notation  $\epsilon_p$ ,  $\epsilon_e$ , and  $\epsilon_B$  for the fractions of energy given to protons, electron and magnetic field respectively, I have in this work assumed  $\epsilon_p = 10/12$  and  $\epsilon_e = \epsilon_B = 1/12$ . This is the same assumption made in Bustamante et al. (2016), and it gives the often used baryonic loading  $\epsilon_p/\epsilon_e = 10$  [4]. The electrons are further assumed to instantaneously radiate their total energy fraction in EM-radiation. The total energy radiated in  $\gamma$ -rays in a GRB is an experimentally determinable quantity, and I therefore require the total  $\gamma$ -ray energy radiated in the simulation to equal the values of  $E_{\gamma,\text{set}}^{\text{iso}}$  given in table 5.1. This is done by determining a scaling coefficient  $C_E$ , through the condition

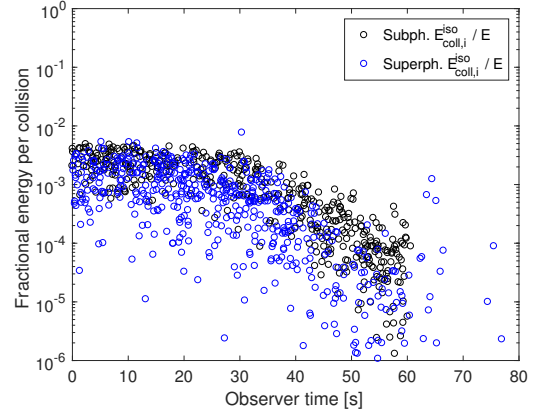
$$E_{\gamma,\text{set}}^{\text{iso}} = C_E E_{\gamma}^{\text{iso,u}} = C_E \sum_{i=1}^{N_{\text{coll}}} E_{\gamma,i}^{\text{iso,u}} = C_E \sum_{i=1}^{N_{\text{coll}}} \epsilon_e E_{\text{coll},i}^{\text{iso,u}}, \quad (5.16)$$

where the sum runs over all collisions, both above and below the photosphere. Once  $C_E$  is obtained, the energies of actual interest are given by

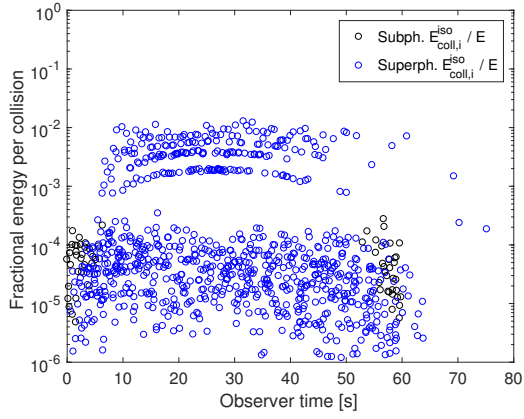
$$E_{\alpha,i}^{\text{iso}} = C_E \epsilon_{\alpha} E_{\text{coll},i}^{\text{iso,u}}, \quad (5.17)$$



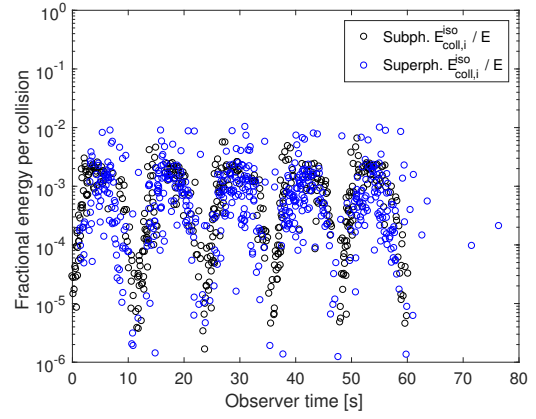
(a) GRB 1



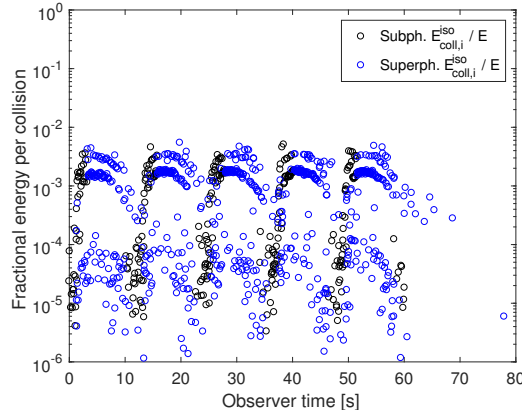
(b) GRB 2



(c) GRB 3



(d) GRB 4



(e) GRB 5

**Figure 5.4:** Fractional energy released per collision as a function of observer time for the five GRBs. One can see the similarity to the initial  $\Gamma$ -distribution for each burst. Collisions marked with black are subphotospheric, and are thus the earliest collisions in the source frame. Evidently, this does not correspond to an earlier observation time in the OF.

where  $\alpha = p, e, B$ . This condition guarantees that the total emitted energy in  $\gamma$ -ray equals  $E_{\gamma, \text{set}}^{\text{iso}}$ . This requirement also makes our choice of initial  $E_{\text{kin}}^{\text{iso}}$  irrelevant, see Appendix A for details. The consequences of such a normalization will be discussed in section 6.2.1.

The magnetic field in the SRF, necessary for the computation of synchrotron cooling of particles, is

$$B'_i \simeq 44.7 \left( \frac{\Gamma_m}{10^{2.5}} \right)^{-1} \left( \frac{\epsilon_B}{\epsilon_e} \right)^{1/2} \left( \frac{E_{\gamma, i}^{\text{iso}}}{10^{50} \text{ erg}} \right)^{1/2} \left( \frac{r_{\text{coll}, i}}{1914 \text{ cm}} \right)^{-1} \left( \frac{l_m}{10^8 \text{ cm}} \right)^{-1/2} \text{ kG}, \quad (5.18)$$

as given by [17]. This translates into a magnetic field energy density as

$$U'_{B, i} = 10^6 \frac{B_i'^2}{8\pi} \text{ erg}. \quad (5.19)$$

### 5.4.3 Proton and photon distributions

The energy released will result in protons and photons with various energies. The likelihood of creating a photon of energy  $\varepsilon$  is given by the photon distribution  $n_\gamma(\varepsilon)$ , with units number of photons per energy and volume. The simulation does not generate the photon or proton spectra. Instead, I use the well established broken power law spectrum for photons, and the power law spectrum characteristic for Fermi acceleration for protons.

The broken power law used for the photon distribution is

$$n'_\gamma(\varepsilon') = C_\gamma \begin{cases} \left( \frac{\varepsilon'}{\varepsilon'_{\text{break}}} \right)^\alpha & \varepsilon' < \varepsilon'_{\text{break}} \\ \left( \frac{\varepsilon'}{\varepsilon'_{\text{break}}} \right)^\beta & \varepsilon' \geq \varepsilon'_{\text{break}}, \end{cases} \quad (5.20)$$

where the slope before the break energy is  $\alpha = -1$  and the slope after is  $\beta = -2$ . The break energy is set to  $\varepsilon'_{\text{break}} = 1 \text{ keV}$  as in Bustamante et al. (2016) [17]. The primes indicate that the distribution is in the SRF. The distributions from each collision  $i$  is then normalized as

$$V'_{\text{iso}, i} \int_{\varepsilon'_{\text{min}}}^{\varepsilon'_{\text{max}}} d\varepsilon' \varepsilon' n'_\gamma(\varepsilon') = \frac{E_{\gamma, i}^{\text{iso}}}{\Gamma_{m, i}}, \quad (5.21)$$

where the RHS is the energy released in the collision in  $\gamma$ -rays in the SRF. The volume  $V'_{\text{iso}, i}$  is of the merged shell and  $\varepsilon'_{\text{min}} = 0.2 \text{ eV}$  and  $\varepsilon'_{\text{max}} = 1 \text{ PeV}$  are the integral limits, taken from [17]. From the equation above, the coefficient  $C_\gamma$  can be determined. In fact, apart from the coefficients, the photon distribution is common to all collisions. Using the terminology  $n'_{\gamma, \text{common}}(\varepsilon') = n'_\gamma(\varepsilon')/C_\gamma$  and  $I = \int_{\varepsilon'_{\text{min}}}^{\varepsilon'_{\text{max}}} d\varepsilon' \varepsilon' n'_{\gamma, \text{common}}(\varepsilon')$ , the coefficients are determined as

$$C_{\gamma, i} = \frac{E_{\gamma, i}^{\text{iso}}}{I V'_{\text{iso}, i} \Gamma_{m, i}} = \frac{E_{\gamma, i}^{\text{iso}}}{I \cdot 4\pi r_{\text{coll}, i}^2 l_{m, i} \cdot \Gamma_{m, i}^2}, \quad (5.22)$$

where  $l_{m, i}$  is the width of the merged shell after collision  $i$ . The extra Lorentz factor appears because of the length contraction of the width in the observer frame:  $l'_{m, i} = l_m \Gamma_{m, i}$ .

The proton distribution is a power law with slope  $-2$  and an exponential cutoff at very high energy. It is given by

$$n'_p(E') = C_p \cdot E'^{-2} e^{-E'/E'_{\text{max}}}. \quad (5.23)$$

The characteristics of the proton distribution is a constant slope that stretches over all energies up to  $E' \sim E'_{\max}$ , where it starts decaying exponentially. The result is that very few/no protons have energies above  $E'_{\max}$ . The maximum energy  $E'_{\max}$  is important for the outcome, and can be found by balancing acceleration rate with synchrotron cooling, and adiabatic and photohadronic energy losses [17], and have been set as in Hümmer et al. (2010) to  $E'_{\max} = 6.9 \cdot 10^8$  GeV. The proton distribution is normalized as the photon distribution in equation (5.21), but with the substitutions  $n'_\gamma(\varepsilon') \rightarrow n'_p(E')$  and  $E_{\gamma,i}^{\text{iso}} \rightarrow E_{p,i}^{\text{iso}}$ , and the coefficients are determined in a similar fashion.

#### 5.4.4 Obtaining neutrino spectra

From the theory in chapters 3 and 4, one can obtain the neutrino spectra from the proton and photon spectra determined in the previous section. The process is pretty straightforward, although tedious. In this subsection, I will make some remarks on my specific approach.

##### Common proton and photon distributions

Even though the simulation generates different distributions for each shell collision, this difference is only in the coefficients  $C_\gamma$  and  $C_p$ ; the energy range and distribution shape will be identical for all collisions. Therefore, it is enough to calculate the pion spectra and resulting neutrino distribution once for  $n'_{\gamma,\text{common}}(\varepsilon')$  and  $n'_{p,\text{common}}(E')$ . This greatly reduces the computational time and is one of the main advantages over a Monte Carlo simulation approach.

##### Resonances

In equation (3.17), there is a double integral that has to be evaluated for each specific pion energy  $E_{\pi,i}$  (subscript  $i$  added to be iterated over to generate the whole pion spectrum, i.e., has nothing to do with a specific shell collision  $i$ ). I approximate this double integral as two log space midpoint Riemann sums:

$$Q_{\pi,i}(E_{\pi,i}) \approx \sum_{j=1}^N \sum_{k=1}^M \frac{N_p(E_j) \Delta E_j}{E_j} n_\gamma(\varepsilon_k) \Delta \varepsilon_k \times \sum_{\text{IT}} \frac{1}{2} \left( \frac{m_p}{E_j \varepsilon_k} \right)^2 \int_{\varepsilon_{\text{th}}}^{\frac{2E_j \varepsilon_k}{m_p}} d\varepsilon_r \varepsilon_r \sigma_{\text{R}}^{\text{IT}}(\varepsilon_r) M^{\text{IT}} \delta \left( \frac{E_{\pi,i}}{E_j} - \chi^{\text{IT}}(\varepsilon_r) \right), \quad (5.24)$$

where the summation upper and lower limits are made to match the integral limits. Please observe that the equation above is in the SRF, where the primes have been omitted for clarity in the equation.

As previously mentioned, the Dirac  $\delta$ -function has the property

$$\delta(g(x)) = \sum_{x_0} \frac{\delta(x - x_0)}{|g'(x_0)|}, \quad (5.25)$$

where  $x_0$  are the zeros of  $g(x)$ . For each pion energy  $E_{\pi,i}$  and proton energy  $E_j$ , the equation

$$g_{ij}^{\text{IT}}(\epsilon_r) = \frac{E_{\pi,i}}{E_j} - \chi^{\text{IT}}(\epsilon_r) = 0, \quad (5.26)$$

has only one solution  $\epsilon_{r,ij}^{\text{IT}}$ , and this solution is obtained by inserting specific energies  $E_{\pi,i}$  and  $E_j$  into equation of interest of (3.31 - 3.34).

The value  $\epsilon_{r,ij}^{\text{IT}}$  has to be compared to the integral limits. Thus, for a specific value of proton energy  $E_j$ , photon energy  $\epsilon_k$  and interaction IT, the contribution to the produced number of pions is

$$Q_{\pi,ijk}(E_{\pi,i})^{\text{IT}} \approx \frac{N_p(E_j)\Delta E_j}{E_j} c \cdot n_\gamma(\epsilon_k)\Delta\epsilon_k \times \frac{1}{2} \left( \frac{m_p}{E_j\epsilon_k} \right)^2 \epsilon_{r,ij}^{\text{IT}} |g^{\text{IT}'}(\epsilon_{r,ij}^{\text{IT}})|^{-1} \sigma_{\text{R}}^{\text{IT}}(\epsilon_{r,ij}^{\text{IT}}) M^{\text{IT}}, \quad \epsilon_{\text{th}} \leq \epsilon_{r,ij}^{\text{IT}} \leq \frac{2E_j\epsilon_k}{m_p}, \quad (5.27)$$

and if  $\epsilon_{r,ij}^{\text{IT}}$  is not within the integral limits, then  $Q_{\pi,ijk}(E_{\pi,i})^{\text{IT}} = 0$ .

In my simulation, I loop over  $i$  and for every iteration I evaluate all  $jk$  combinations for each of the nine resonances. As this is a double sum, the complexity and simulation time for each iteration scales as  $N \times M$ , but the code is quite fast so for  $N, M < 1000$ , it is fine ( $\sim 0.7$  s for each iteration  $i$  when  $N = M = 1000$ ).

## Direct and multipion production

The contribution from direct production and multipion production is given by equation (3.47). As the  $\delta$ -function has been used to remove the integral over proton energies, and the integral over  $\epsilon_r$  has been replaced by a polynomial in both cases, there is only one integral left to compute. As with resonances, this is done by approximating the integral as a logspace midpoint Riemann sum

$$Q_\pi(E_\pi) = N_p \left( \frac{E_\pi}{\chi^{\text{IT}}} \right) \cdot c \sum_{k=1}^M \Delta\epsilon_k n_\gamma(\epsilon_k) \times \sum_{\text{IT}} \frac{1}{2} \left( \frac{m_p \chi^{\text{IT}}}{\epsilon E_\pi} \right)^2 \frac{M^{\text{IT}}}{\chi^{\text{IT}}} f^{\text{IT}} \left( \frac{2E\epsilon}{m_p} \right). \quad (5.28)$$

This complexity scales as  $M$  and thus these contributions are much faster to compute. Once again, the above equation is in the SRF even though the primes have been omitted.

## Time integration of production rate

In chapter 3, I obtained the expressions for the production rate of pions. To get the total number of pions created, one has to integrate over time. I have taken this time to be the average time for photons to escape the shell in which they were created. The escape time for radiation created after shell collision  $i$  calculated in the OF, is the time it takes the radiation to catch up with the shell's front boundary

$$t_{\text{esc},i} = \frac{\langle d_i \rangle}{c - v_{\text{m},i}} = \frac{l_{\text{m},i}}{2(c - v_{\text{m},i})} = \frac{l_{\text{m},i}}{2c(1 - \beta_{\text{m},i})} \approx \frac{l_{\text{m},i}\Gamma_{\text{m},i}^2}{c}, \quad (5.29)$$

where the  $\langle d_i \rangle$  is the average distance radiation has to the shell's front boundary, assumed to be  $l_{m,i}/2$ . In the equation above, I have assumed the radiation to travel along the line of sight, which is justified in the OF. The radiation in a GRB will be beamed towards Earth, else it would not be observable at all. The beaming angle is proportional to  $\Gamma^{-1}$  so all GRBs are strongly beamed. Radiation traveling outside the cone with opening angle  $1/\Gamma$ , will travel towards regions with higher opacity. The reason is simple: radiation in the beaming direction travels along the flow of electron while radiation outside of the beaming cone travel against the electron flow, and are therefore much more likely to scatter. For collisions just above the photosphere, the most important collisions for neutrino production, the opacity increase outside of the beaming cone is so quick, that photons traveling in this direction can be assumed to scatter instantaneously. In this scattering, the probability of radiating outside the beaming cone will be suppressed once again. Thus, in collisions above the photosphere, almost all radiation will end up traveling along the line of sight, and one can assume they do so instantaneously.

The time elapsed in the SRF will be dilated by a factor  $\Gamma^{-1}$  and so the total number of produced pions for collision  $i$  is given by multiplying the production rate with the average escape time in the SRF:

$$N'_{\pi,i}(E'_\pi) = Q'_{\pi,i}(E'_\pi) \cdot t_{\text{esc},i} \Gamma_{m,i}^{-1} = \frac{l_{m,i} \Gamma_{m,i}}{c} Q'_{\pi,i}(E'_\pi). \quad (5.30)$$

In the observer frame, the spectral shape is of course identical, but shifted towards higher energies with a factor of  $\Gamma_{m,i}$ .

In this simplified approach, I have not taken into account what I call secondary photohadronic interactions; photohadronic interaction between protons and photons from different shells. I will discuss what effect including this would have on the outcome in section 6.2.5.

### 5.4.5 Implemented photosphere

The expression for the photospheric radius derived in the background chapter is obtained by integrating from  $r$  to infinity for the optical depth. This indicates that a photon created at  $r$  must reach infinity to be regarded as having escaped. This approach is well suited for a continuous outflow, where the interaction probability is non-zero at all points in space. However, in the discrete outflow used in my simulation, one can instead define escape as the photon reaching the edge of the shell in which it was created. Assuming a photon emitted on the line of sight, the expression for optical depth is then instead

$$\tau = \int_{r_{\text{coll}}}^{r_{\text{esc}}} n'_e \sigma_{\text{T}} \Gamma (1 - \beta) dr'. \quad (5.31)$$

Assuming collisions occur sufficiently far out in the jet, the electron density will have decreased to a point where it remains roughly constant during the light escape timescale, and can then be taken outside of the integral:

$$\tau = n'_e \sigma_{\text{T}} \Gamma (1 - \beta) \int_{r_{\text{coll}}}^{r_{\text{esc}}} dr' = \frac{n'_e \sigma_{\text{T}}}{2\Gamma} (r_{\text{esc}} - r_{\text{coll}}). \quad (5.32)$$

As previously, I assume that the electron density can be associated with the proton density and the proton density of shell  $k$  is

$$n'_p = \frac{m_k}{m_p V'_{\text{iso},k}} = \frac{m_k}{4\pi r^2 l'_k m_p}. \quad (5.33)$$

The escape radius for shell  $k$  is given by  $r_{\text{esc},k} = r_{\text{coll}} + ct_{\text{esc},k}$ . The average escape time for photons was found in equation (5.29) so the escape radius is

$$r_{\text{esc},k} = r_{\text{coll}} + l_k \Gamma_k^2 = r_{\text{coll}} + l'_k \Gamma_k. \quad (5.34)$$

Inserting this expression into equation (5.32) yields

$$\tau_k = \frac{n'_e \sigma_{\text{T}}}{2\Gamma_k} (l'_k \Gamma_k) = \frac{m_k \sigma_{\text{T}}}{8\pi r^2 m_p}. \quad (5.35)$$

Once again, the photospheric radius is defined as  $\tau(r_{\text{ph}}) = 1$ , so for shell  $k$  one gets  $r_{\text{ph},k}$  as

$$r_{\text{ph},k} = \sqrt{\frac{\sigma_{\text{T}} m_k}{8\pi m_p}} \approx 1.627 \times 10^{-13} \sqrt{\frac{m_k}{m_p}} \text{ cm}. \quad (5.36)$$

One important thing to notice, is that  $m_k$  needs to be scaled with the energy coefficient  $C_E$  as well, as  $m_k \propto E_{\text{kin}}^{\text{iso}}$ . This means that if  $r_{\text{ph},k}$  are calculated with initial masses, it has to be multiplied by a factor  $C_E^{1/2}$ .

The photosphere is the surface of the last scattering, above which the plasma in the shell becomes optically thin. As I have adapted a photon distribution shape to mimic observed  $\gamma$ -ray spectra from real GRBs, and as such data will mainly come from super-photospheric collisions per definition, it is not justifiable to assume a similar shape below the photosphere. Therefore, the results in this thesis will be based on collisions above the photosphere only. It will be discussion in section 6.2.2 how including effects from below the photosphere would influence the results.

In figure 5.5, we can see the energy output in  $\gamma$ -rays and neutrinos as a function of radii. Subphotospheric  $\gamma$ -ray energies are shown in cyan, while  $\gamma$ -ray energies from collisions above the photosphere are shown in blue. Neutrino energies shown in red are from collisions above the photosphere only.

#### 5.4.6 Gamma-ray pulse per collision and observed light curve

For each shell collision a  $\gamma$ -ray pulse is emitted by the cooled electrons. The pulse shape can be parametrized as in Kobayashi et al. (1997) [6]. If the first observed light from a collision  $i$  above the photosphere is at  $t_{\text{obs},i}$ , then the flux at Earth is given by

$$F_{\gamma,i}(t) = \frac{1}{4\pi d_L(z)^2} \times \begin{cases} 0 & t < t_{\text{obs},i} \\ h_i \left[ 1 - \left( 1 + \frac{2\Gamma_{m,i}^2 ct}{(1+z)r_{\text{coll},i}} \right)^{-2} \right] & t_{\text{obs},i} \leq t < t_{\text{obs},i} + t_{\text{rise},i} \\ h_i \left[ \left( 1 + \left( \frac{2\Gamma_{m,i}^2 t}{1+z} - \delta t_{e,i} \right) \frac{c}{r_{\text{coll},i}} \right)^{-2} - \left( 1 + \frac{2\Gamma_{m,i}^2 ct}{(1+z)r_{\text{coll},i}} \right)^{-2} \right] & t \geq t_{\text{obs},i} + t_{\text{rise},i}, \end{cases} \quad (5.37)$$

where  $d_L(z)$  is the luminosity distance to Earth for redshift  $z$  and  $t$  is the time in the OF. If collision  $i$  instead occurred below the photosphere, its contribution is discarded by setting  $F_{\gamma,i} = 0$ . The redshift  $z$  was set to 2, and assuming a flat universe,  $\Omega_{\Lambda} = 0.714$ ,

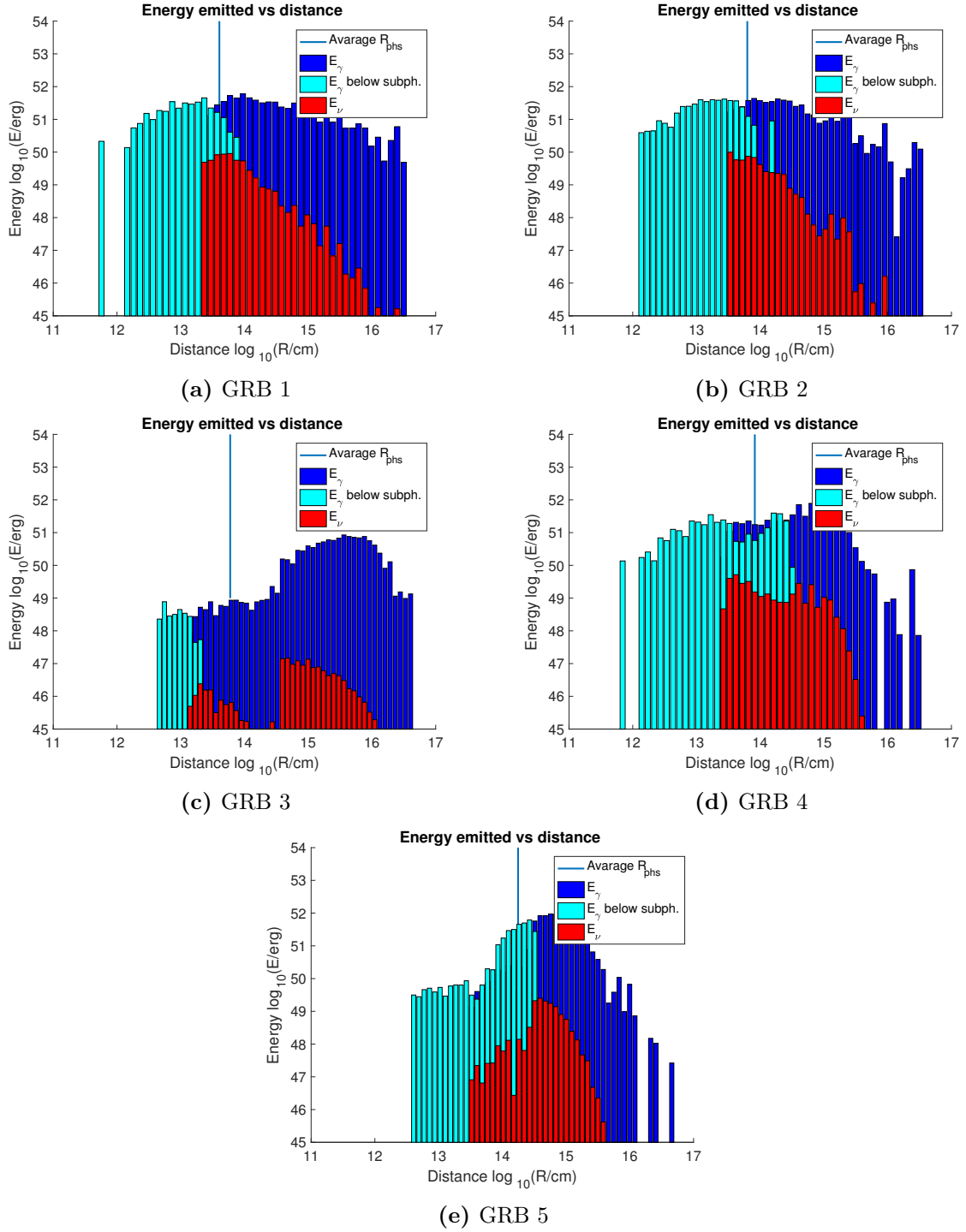


**Figure 5.5:** Energy released in  $\gamma$ -rays and neutrinos for each burst. Subphotospheric  $\gamma$ -ray energies are shown as well. All GRBs but GRB 3 have strongest neutrino emittance close to the photosphere. Picture inspiration taken from Bustamante et al. (2016) [17].

$\Omega_m = 0.286$ , and  $H_0 = 69.6$  (km/s)/Mpc, the luminosity distance to Earth was calculated to  $d_L(2) = 51.594$  Gly [19]. The emission timescale  $\delta t_{e,i}$  is given by the time it takes the reverse shock to cross the fast shell

$$\delta t_{e,i} \equiv \frac{l_f}{c(\beta_f - \beta_{rs})}. \quad (5.38)$$

The pulse peak height  $h_i$  is given by

$$h_i = \frac{E_{\gamma,i}^{\text{iso}}}{(1+z)t_{\text{rise},i}}, \quad (5.39)$$

where the rise time, defined as the time it takes to reach the pulse peak height, is given by

$$t_{\text{rise},i} \equiv \frac{\delta t_{e,i}}{2\Gamma_{m,i}^2}(1+z). \quad (5.40)$$

The observed light curve is obtained as a superposition of the pulses from all collisions

$$F_\gamma(t) = \sum_{i=1}^{N_{\text{coll}}} F_{\gamma,i}. \quad (5.41)$$

# Chapter 6

## Results and discussion

In this chapter, I will present my results and discuss how this should be interpreted and how one can improve upon my work to refine the results.

### 6.1 Results

As mentioned in the beginning of this thesis, one of the most intriguing things about GRBs are their vast difference in observed light curve shapes. The light curves, together with the corresponding neutrino light curves for each of the five GRBs, can be seen in figure 6.1. Plotted in the figure are the observed light curves for photons, obtained through the method described in subsection 5.4.6. For the neutrino light curve, the same process has been used. The total neutrino energy in each collision  $i$  was calculated as

$$E_{\nu,i}^{\text{iso}} = \int_0^{\infty} dE_{\nu} E_{\nu} N_{\nu,i}(E_{\nu}), \quad (6.1)$$

where energies are in the OF and  $N_{\nu,i}$  includes all neutrino flavors. From the figure, one can see that the simulation manages to get pretty diverse curve shapes. GRB 1 has a high variability but a static mean value, as one would expect from initial  $\Gamma$  randomized around the same mean. GRB 2 and GRB 3 both exhibit a shape somewhat similar to FRED (fast rise exponential decay) although GRB 2 has a lot of variability which GRB 3 seems to lack almost completely. GRB 4 and GRB 5 both show periodic behavior, which again is not surprising if one remembers the oscillating progenitors they are supposed to imitate. GRB 5 have fewer spikes than GRB4, due to fewer collisions above the photosphere.

In figure 6.2, the predicted all sky fluxes  $J_{\nu_{\mu}}$  for each GRB can be seen. Assuming a rate of 667 GRBs per year, one can get a prediction of the all sky flux by scaling the result from the GRB of interest with the event rate:

$$J_{\nu_{\mu}}^{\text{GRB}j}(E_{\nu}) = \frac{N_{\nu_{\mu}}^{\text{GRB}j}(E_{\nu})}{4\pi d_L(z)^2} \frac{667}{4\pi} \text{yr}^{-1} \text{sr}^{-1}, \quad (6.2)$$

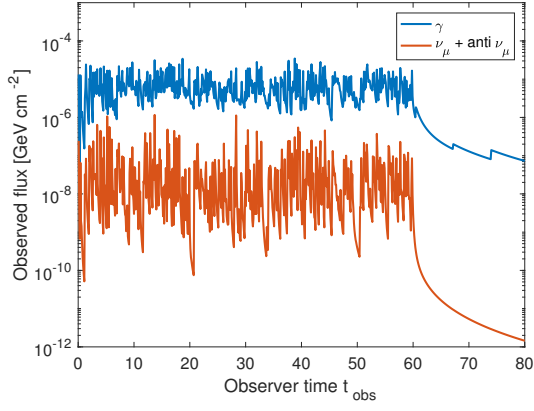
where  $N_{\nu_{\mu}}^{\text{GRB}j}(E_{\nu})$  is the sum of all  $\nu_{\mu}$  and  $\bar{\nu}_{\mu}$  created in shell collisions above the photosphere for GRB  $j$ ,  $d_L(z)$  is still the luminosity distance, and the extra factor of  $4\pi$  appears to get the flux per steradian. The shape is similar for all GRBs. It is characterized by a quite broad peak, centered around  $10^7$  GeV. Shown in each subfigure is

the IceCube 2017 upper limit [4] for comparison. Only the weakest neutrino emitters GRB 3 and GRB 5, are below the upper limit. GRBs 1 and GRB 2 are the strongest neutrino emitters with peak heights at  $7 \times 10^{-10} \text{ GeVcm}^{-2}\text{s}^{-1}\text{sr}^{-1}$ , and GRB 4 with a peak height of  $4 \times 10^{-10} \text{ GeVcm}^{-2}\text{s}^{-1}\text{sr}^{-1}$  is the third strongest. GRB 3 is the weakest neutrino emitter with a peak height of more than two orders of magnitude less than the others at  $5 \times 10^{-13} \text{ GeVcm}^{-2}\text{s}^{-1}\text{sr}^{-1}$ . The solid lines shown in each subfigure are the shell collisions that contributes most to the flux.

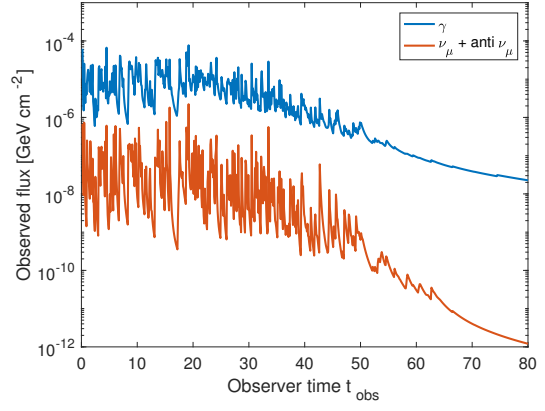
As no one of the benchmarks can imitate all recorded GRBs alone, I have also included the average all sky flux in figure 6.3, as a slightly more realistic approach. There, I assume that GRBs 1 to 5 contribute one fifth each to the yearly rate. In this figure, the 2016 upper limit computed by the IceCube collaboration, shown in figure 6 in [17], has been included as well for reference. All GRBs are below the 2016 limit, but as already seen, only GRB 3 and 5 are below the 2017 limit. The average calculated flux peaks at  $\sim 4 \times 10^{-10} \text{ GeVcm}^{-2}\text{s}^{-1}\text{sr}^{-1}$  and is above the 2017 limit by a factor  $\sim 2$ . As this limit is set with a confidence level of 90 %, this result disfavors the internal shock model as the main process behind GRB energy dissipation. This result is only valid under my current assumptions though, see section 6.2.4.

In figure 6.4 every hundredth shell collision above the photosphere is plotted. The subfigures show the evolution of neutrino fluxes during each of the five bursts. A general tendency seems to be that earlier collisions have higher total fluxes peaked at lower energies. This is easy to explain. The earlier collisions are more likely to happen at small  $r$ , where both photon density  $n_\gamma$  and magnetic field energy density  $U'_B$  are higher. Higher photon density leads to more created pions that subsequently can decay to more neutrinos pushing up the flux. A higher magnetic field energy density however, makes the created pions and muons cool quicker, and thus they loose more of their energy. This shifts the peak to lower energies, even though the total flux is still higher than for collisions happening at larger  $r$ .

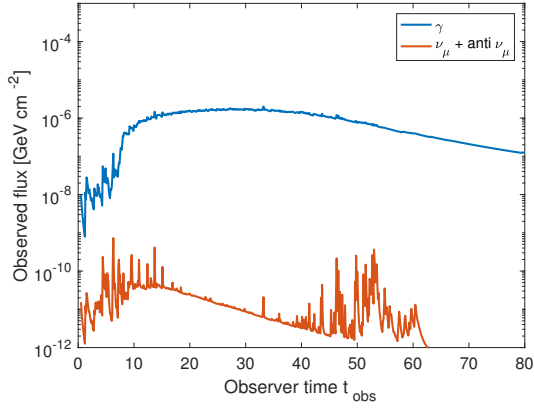
This behavior is also seen in figure 6.5, where it is clearly visible how the neutrino flux decreases as a function of collision radii. The red line marks an  $r^{-2}$  slope. It can be seen in subfigure 6.5a that the fluxes deviates from this  $r^{-2}$  dependence, with a slightly less steep slope. This is due to a weaker  $U'_B$  further out and so less cooling losses. The behavior in the other subfigures are not as easily determined. GRBs 3 and 5 (subfigures 6.5c and 6.5e) have similar behavior, with high energy collisions occurring far out. There are downwards curling patterns that clearly stand out amidst the other, more randomly distributed dots. Remembering the initial  $\Gamma$ -distributions, GRB 3 and 5 both oscillated with little spread. The visible patterns come from the shells with the highest  $\Gamma$  at the peaks of the pulses, having caught up with the slowest shells in the pulse valleys. As the initial distribution spread is low, they all catch up at almost the same radii. One can compare the radii at which this occurs for GRB 5, to the  $\Gamma$ -distribution shape in figure 5.2 after 500 collisions. As GRB 3 only has one pulse this behavior occurs much further out.



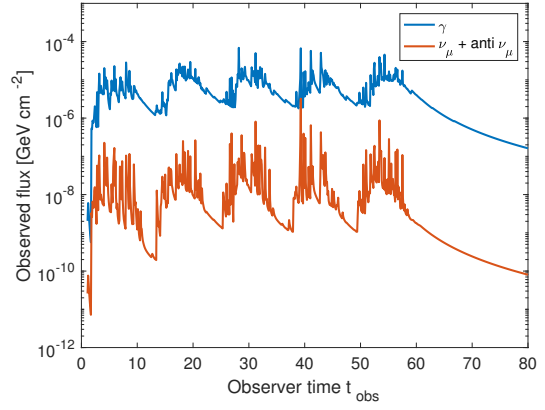
(a) GRB 1



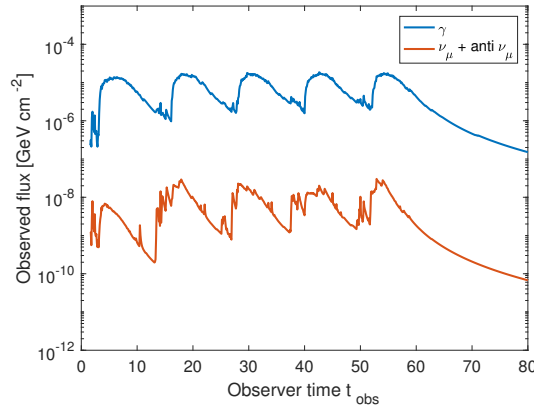
(b) GRB 2



(c) GRB 3



(d) GRB 4



(e) GRB 5

**Figure 6.1:** The  $\gamma$  and neutrino light curves as observed on earth for  $z = 2$  for the five benchmark GRBs. Neutrino light curves include contributions from both  $\nu_\mu$  and  $\bar{\nu}_\mu$ . Figure inspiration taken from Bustamante et al. (2016) [17].

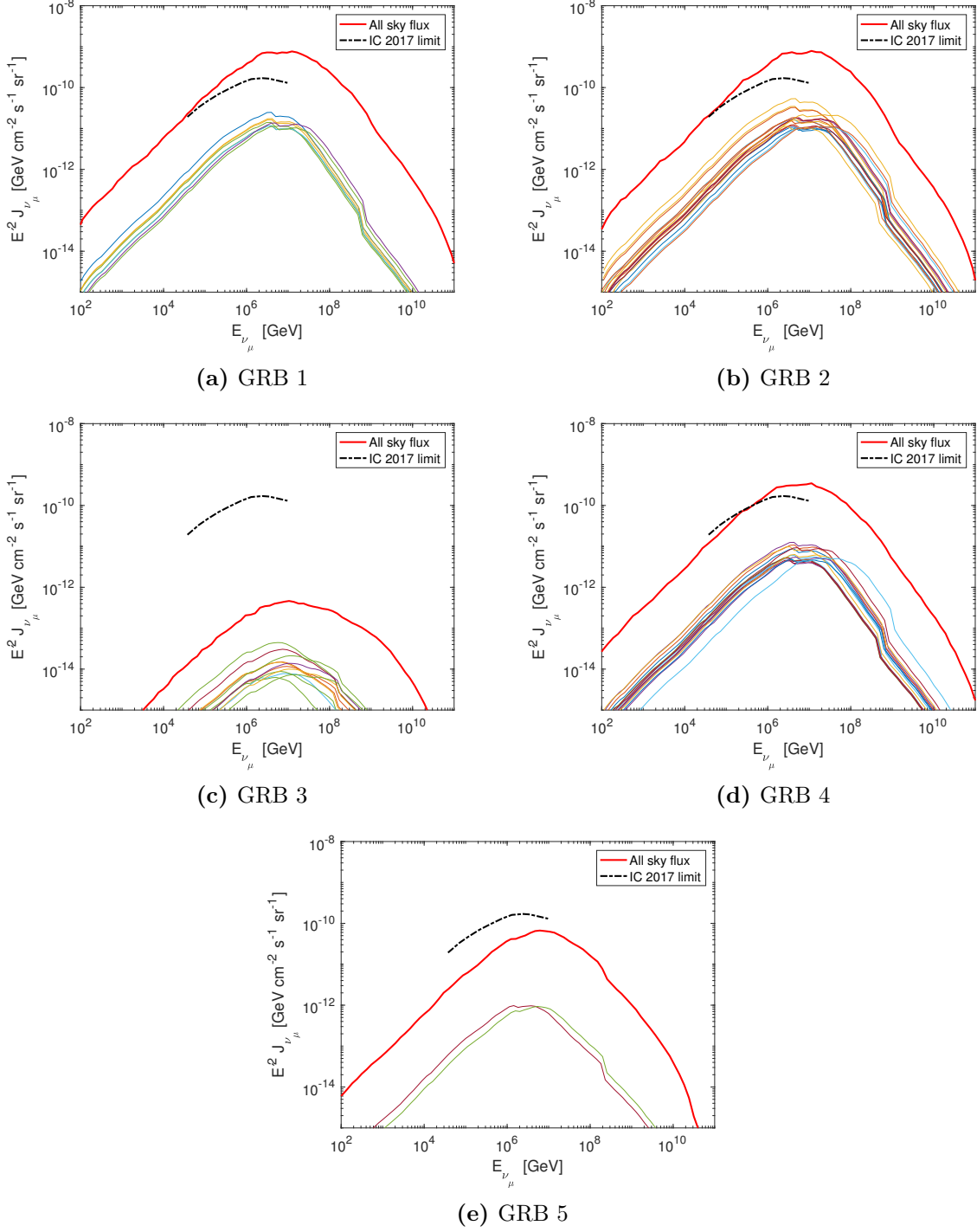


**Figure 6.2:** Computed all sky flux of  $\nu_\mu + \bar{\nu}_\mu$  from the different GRBs, showed as red lines. The solid lines below are the distributions from the most contributing shell collisions. The black dotted line is the IceCube collaboration's upper limit with 90 % CL [4]. Figure inspiration taken from Bustamante et al. (2016) [17].

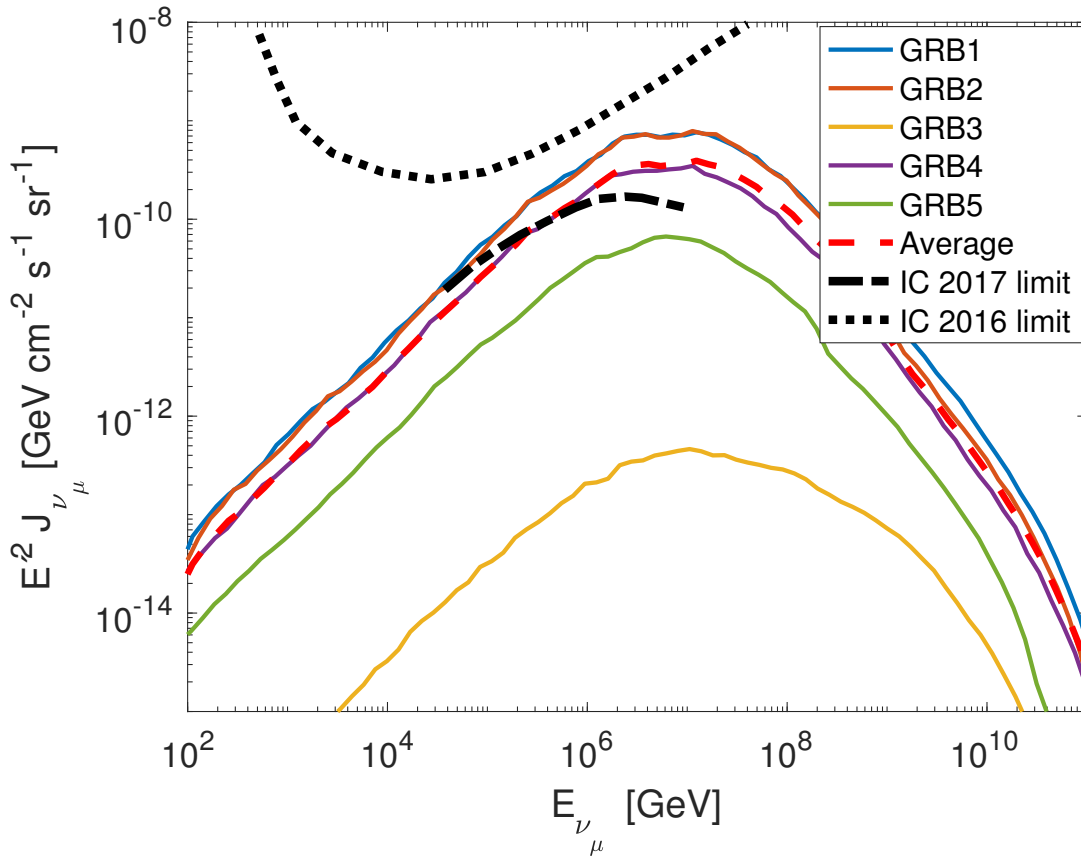


**Figure 6.3:** Predicted all sky fluxes from all five GRBs together with their average, shown as a red dashed line. The IceCube collaboration’s 2017 upper limit as well as their 2016 upper limit are shown [4,17].

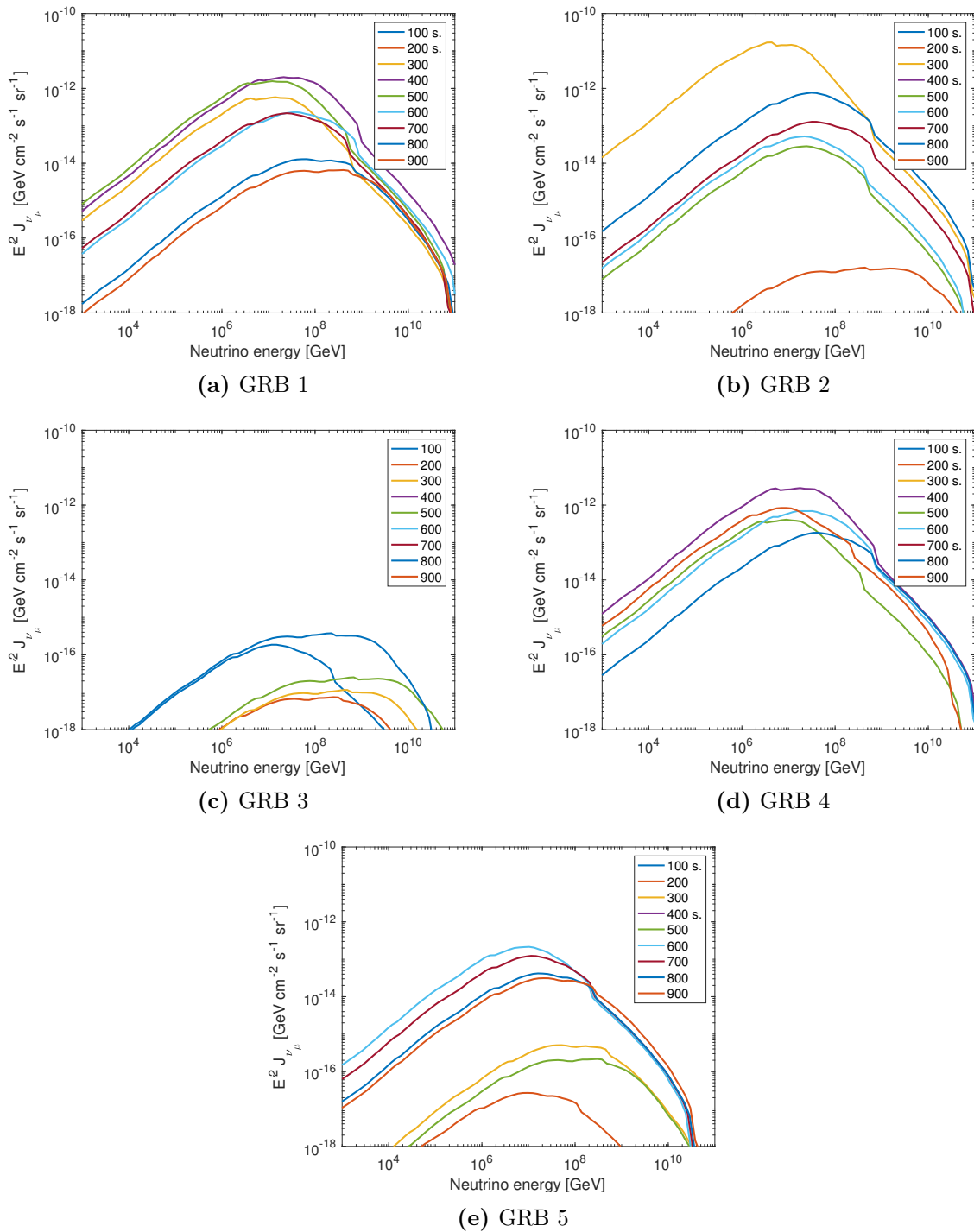


**Figure 6.4:** Plot of how much every hundredth collision above the photosphere contributes to the computed all sky flux. Gives an indication of the shell collision evolution of the burst. The legend indicates collision number, and subphotospheric collisions are marked with an s.

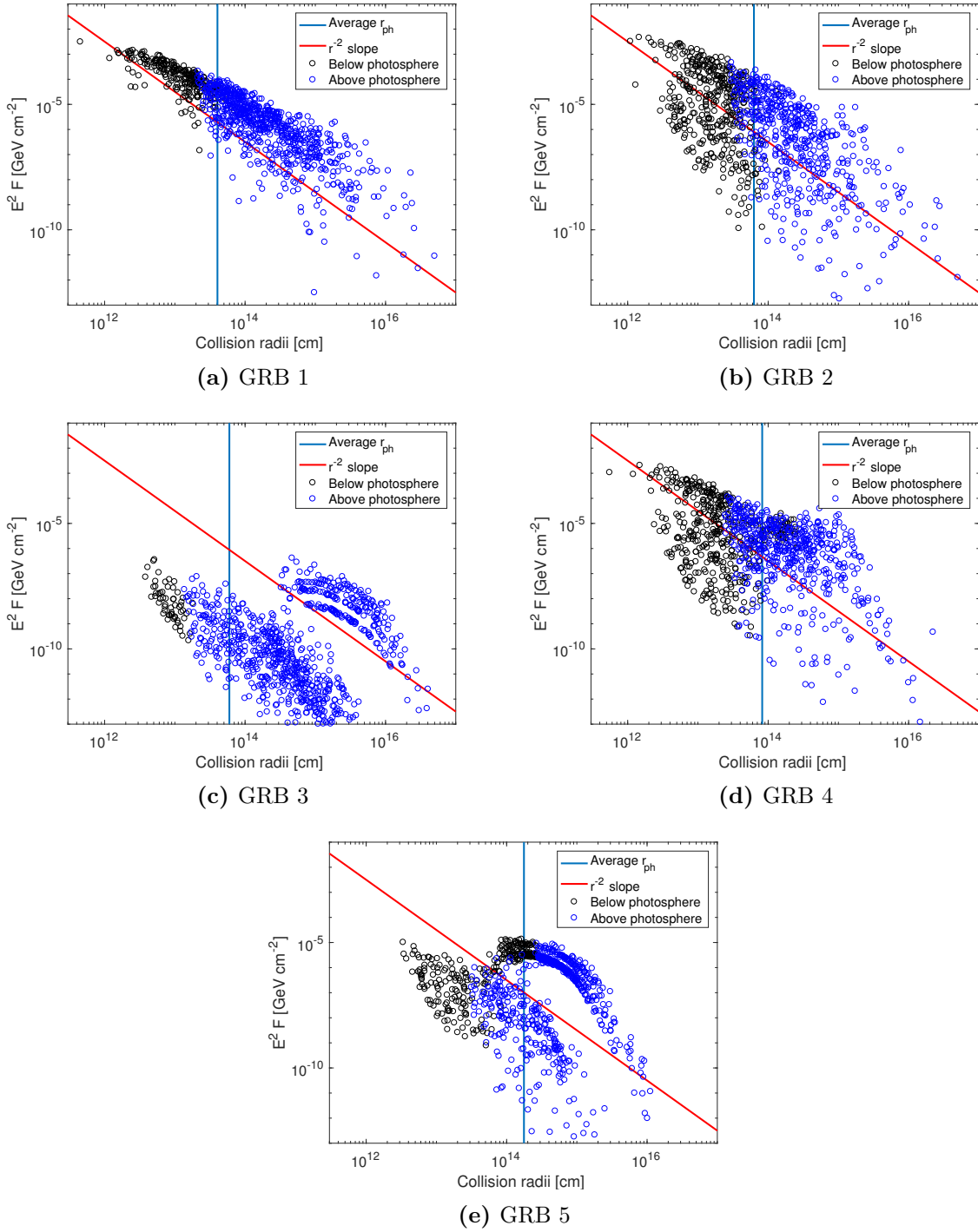


**Figure 6.5:** Neutrino flux as a function of collision radii for the five bursts. Black circles mark subphotospheric collisions while blue circles are superphotospheric collisions. The average photospheric radius has been marked. The red line shows an  $r^{-2}$  slope. Figure inspiration taken from Bustamante et al. (2016) [17].

## 6.2 Discussion

The results obtained in this thesis give good predictions of the neutrino fluxes observable at earth from different types of GRBs. However, there are limits to the model and improvements that can be made. Some of them will be discussed in this section.

### 6.2.1 Energy scaling and initial $\Gamma$ spread

In the simulation I scale the emitted radiation, as already mention in equation (5.16), by determining a scaling coefficient  $C_E$  as

$$C_E = \frac{E_{\gamma,\text{set}}^{\text{iso}}}{E_{\gamma}^{\text{iso,u}}}, \quad (6.3)$$

where  $E_{\gamma}^{\text{iso,u}}$  is defined as

$$E_{\gamma}^{\text{iso,u}} = \sum_i^{N_{\text{coll}}} \epsilon_e E_{\text{coll},i}^{\text{iso,u}}. \quad (6.4)$$

While this has the advantage of scaling the emitted energy in  $\gamma$ -rays to something that is actually observable, it also poses some problems.

What is effectively being done, is a scaling of the total energy emitted by the progenitor with a factor  $C_E$ . As described in Appendix A,  $E_{\text{coll},i}^{\text{iso,u}}$  is directly proportional to the choice of  $E_{\text{kin}}^{\text{iso}}$ . As the total emitted energy from the progenitor is

$$E_{\text{tot}}^{\text{GRB}} \approx E_{\text{kin}}^{\text{iso}} N_{\text{shells}}, \quad (6.5)$$

the effect of scaling the individual collisions is to scale the total energy emitted by the progenitor. With  $E_{\text{kin}}^{\text{iso}} = 10^{51}$  erg, this is no problem as long as  $C_E \sim 1$ . To acquire  $C_E \sim 1$  however, one has to have effective energy conversion. This is why the initial  $\Gamma$  need to have such a large spread (see figure 5.1). This is a well known problem with the internal shock model, that for effective energy conversion to be possible,  $\Gamma_{k+1}/\Gamma_k \gg 1$  in a collisions between shells  $k$  and  $k+1$ . For less extreme distributions as can be seen in figure 6.6 (initial values given in table 6.1), the coefficients become  $C_E^6 = 239$  and  $C_E^7 = 21$ , resulting in  $E_{\text{tot}}^{\text{GRB}6} = 2.4 \cdot 10^{56}$  and  $E_{\text{tot}}^{\text{GRB}7} = 2.1 \cdot 10^{55}$ , both unrealistically high. Thus, the validity of the simulation relies on the central engine being able to create such large variety, something which might be questionable [3].

Due to the large values of  $\sigma^{\text{logn}}$  in GRBs 1, 2, and 4, they all have shells with bulk Lorentz factor  $\Gamma$  reaching almost  $10^4$ , which is much to high. As a more realistic approach, those three GRBs were run again with an upper threshold of  $\Gamma^{\text{th}} = 1000$ ; if a random value was generated with  $\Gamma_{k,0} > \Gamma^{\text{th}} = 1000$ , the simulation was told to generate a new value for  $\Gamma_{k,0}$ . The result can be seen in figure 6.7. All three GRBs have a significantly lower flux than before, even though they are all still over the IceCube 2017 upper limit.

### 6.2.2 Effects of subphotospheric collisions

As is evident from figure 6.5, the largest energy contributions often come from shell collisions just above the photosphere. As previously mentioned, this work completely discard all collisions below the photosphere. Although the distributions I have given to

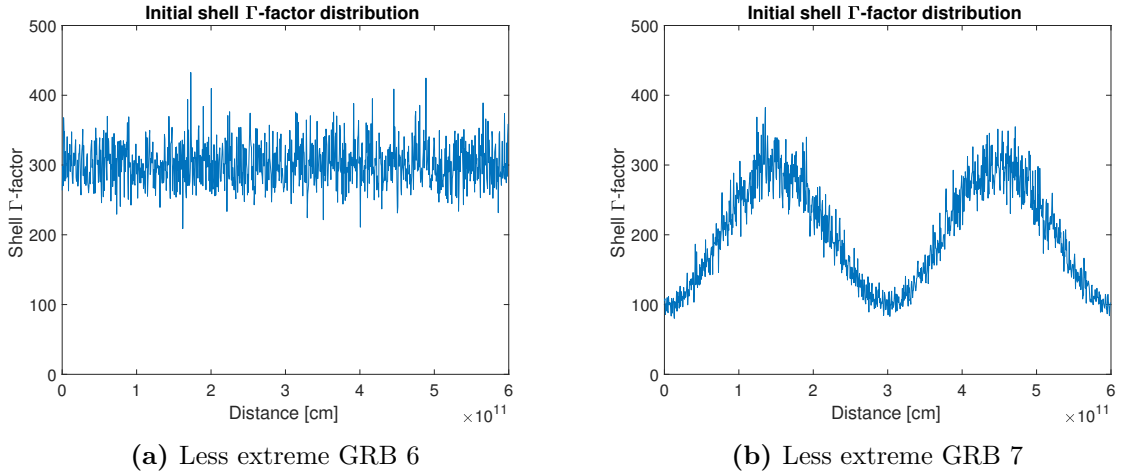


**Figure 6.6:** Two less extreme initial distribution of  $\Gamma$ .

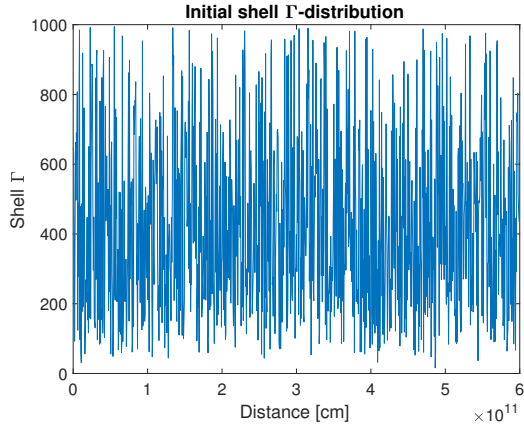
protons and photons is not valid below the photosphere, photohadronic interactions will probably still occur to some extent. Because the neutrinos are only weakly interacting, those that are produced below the photosphere will be able to escape the plasma and contribute to the neutrino flux. However, for any extensive amount of neutrino production to occur, one needs highly relativistic protons, and the question is if protons can be accelerated to such high energies below the photosphere. If the collision occurs where the optical depth is very high, the charged particles will be so tightly bound to the photons that no major acceleration can take place. If there is an intermediate region close to the photosphere, in which protons could be accelerated while  $\tau > 1$  still, collisions here could possibly contribute to the observed flux. As the optical depth is very quickly decreasing with  $r$ , this has to be a narrow region though.

The radiation trapped in shell collisions below the photosphere would raise the internal energy of the shell. Because the shell is optically thick, the photon spectrum is similar to one from a blackbody. the thermal radiation created below the photosphere could shape the photon distribution to one with a power law spectra in the high energy band, and a thermal contribution to the lower energies [20]. If a first generation merged shell, a shell that have interacted once, were to collide just above the photosphere again, is is reasonable to believe that its thermal radiation resulting from the previous collisions could contribute to the neutrino flux. As the total flux is dominated by collisions close to  $r_{\text{ph}}$ , this might have effect on the result. That many collisions like this would occur seems implausible however, as the collision frequency is much lower than the timescale at which the shell cools once it reaches  $r_{\text{ph}}$ .

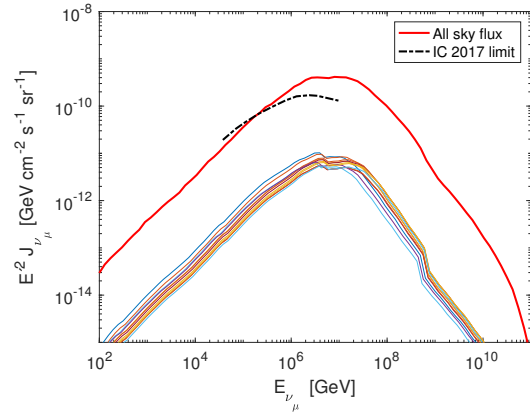
If any of these two aspect would influence the results, it would be in increasing the calculated flux. Thus, the fluxes shown in figure 6.2 should be considered lower bounds.

**Table 6.1:** Less extreme GRB parameter inputs.

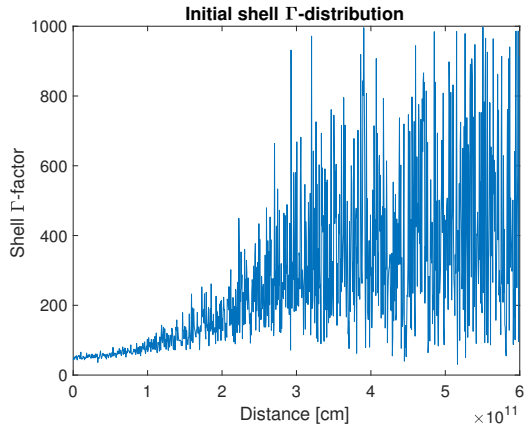
GRB	$\Gamma_{0,1}$	$\Gamma_{0,2}$	$\sigma_{0,1}^{\text{logn}}$	$\sigma_{0,2}^{\text{logn}}$	$N_{\text{osc}}$	$E_{\gamma,\text{set}}^{\text{iso}}$
6	300	-	0.1	-	-	$10^{53}$
7	100	300	0.1	0.1	4	$10^{53}$



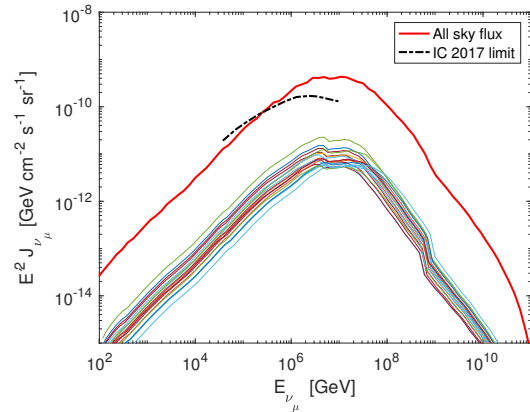
(a)  $\Gamma$ -distribution of GRB 1 with upper threshold



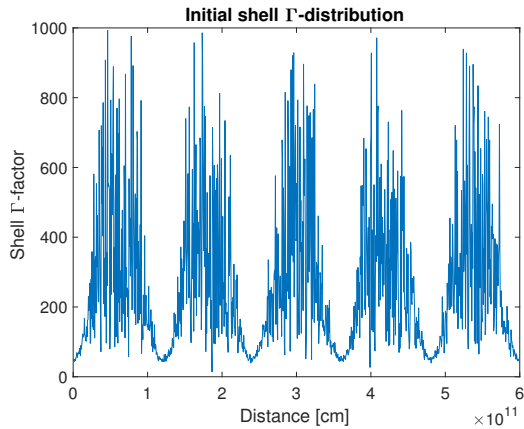
(b) Predicted all sky flux GRB 1



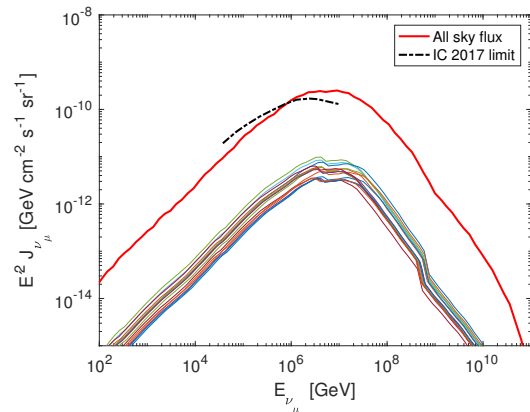
(c)  $\Gamma$ -distribution of GRB 2 with upper threshold



(d) Predicted all sky flux GRB 2



(e)  $\Gamma$ -distribution of GRB 4 with upper threshold



(f) Predicted all sky flux GRB 4

**Figure 6.7:** GRBs 1, 2, and 4 with an upper threshold to the initial shell bulk Lorentz factor, set to  $\Gamma^{\text{th}} = 1000$ . The new  $\Gamma$ -distributions are shown to the left, with the resulting predicted all sky flux to the right. Although, all fluxes have decreased, they are still above the IceCube 2017 limit [4].

### 6.2.3 External contributions

In this work, I have not considered any contributions further out than  $r_{\text{cbm}}$ , so called external contributions. The density of protons and photons is so low at these radii, that photohadronic interactions are much less significant. Furthermore, the simulation is set up so that  $N_{\text{coll}} \lesssim N_{\text{shells}}$ , so the number of shells that reaches  $r_{\text{cbm}}$  are only a few tens at the most. Neutrino production during the afterglow is not within the scope of this thesis. During the afterglow, there will be low densities but much more time for interactions to occur, which is quite the opposite of what I have studied. This could be interesting to include in future research. Including external contributions would raise the flux, so again my computed fluxes could be seen as lower bounds.

### 6.2.4 Varying assumptions

It is important to note the many assumptions made in this work. The simplifications made when calculating the neutrino flux should not have any significant impact on the result (see Hümmer et al. (2010) [8] for comparisons between their method and Monte Carlo simulations). However, there are several quantities in my simulation that are not predicted by the simulation itself, but are decided by the user, and the chosen values of these quantities have large influence. In this subsection, I will motivate some of the choices made, and also expand on how varying the parameters would effect the result. As the simulation was made to mimic Bustamante et al. (2016) [17], many numerical parameter values have been copied from them directly.

The radius of the innermost shell is set to  $r_{\text{inner}} = 10^8$  cm. This is the same assumption made in [17], and it is of the same order as the initial widths of the shells  $r_{\text{inner}} \sim l_0$ . The interpretation is that the simulation is set to start once the final shell has been emitted by the progenitor. As the shells in a GRB are accelerated up to the coasting radius  $r_s$ , and as each shell in the simulation is given a constant  $\Gamma$  to begin with, the simulation might more appropriately start at  $r_{\text{inner}} = r_s$ . The coasting radius can be approximated as  $r_s \sim \Gamma l_0 \sim 10^{11}$  cm. The effect of changing  $r_{\text{inner}}$  is just to push all collisions further out by a constant, and as the most important collisions happen at a collisions radii of  $r_{\text{coll}} \gtrsim 2 \times 10^{13}$  cm, the effect of adding  $10^{11}$  cm is negligible.

Assumptions that do have significant influence are the values of the fractions  $\epsilon_p$ ,  $\epsilon_e$ , and  $\epsilon_B$ . The limiting factor are the number of available energetic protons, so a change of the baryonic loading  $1/f_e = \epsilon_p/\epsilon_e$  directly scales the predicted neutrino flux. A great visual example of this is shown in figure 3 in Hümmer et al. (2012) [18]. In this thesis, I have used the value  $1/f_e = 10$ , as it seems to be a popular value in the literature [4,17,18], but this value is not certain. Lowering the baryonic loading to  $1/f_e = 1$  decreases the all sky flux significantly. GRB 1, and 2 are still above the IceCube 2017 limit but barely, while GRB 4 is then below. Keeping the baryonic loading constant, but increasing the energy given to magnetic field decreases the flux as well, because the pions and muons are more effected by synchrotron cooling. Increasing the magnetic field in the shock would effect the initial proton distribution however, and as this is not something I have taken into account here, these results should be treated with care.

Similarly to the energy fractions, the result relies a lot on the choice of  $E_{\gamma,\text{set}}^{\text{iso}}$ . This is hardly surprising; increasing  $E_{\gamma,\text{set}}^{\text{iso}}$  scales the amount of energy given to both protons and photons. It is not a direct proportionality though, as the energy given to magnetic field increases as well, leading to higher cooling losses.

The way the photospheric radius is calculated outlined in subsection 5.4.5, results in an unusually large  $r_{\text{ph}}$ . A large value of  $r_{\text{ph}}$  effectively lowers the fluxes. Implementing a photospheric radius as described in the background, section 2.2, yields fluxes 1-2 orders of magnitude higher. The peaks are also shifted to lower energies in this case, due to higher  $U'_B$  at lower radii.

The redshift has been set to  $z = 2$ , just as in Bustamante et al (2016). In the calculation of the all sky fluxes seen in figure 6.2, all GRBs are assumed to occur at same  $z$ . Although  $z = 2$  is close to the average redshift for GRBs, this is of course a naive assumption. A more refined model can be found in Baerwald et al. (2012) [21], where they study the GRB rate as a function of redshift, as well as the effect of varying redshift on neutrino production. As the neutrino fluxes scale as  $d_L(z)^2$  (see equation (5.37)), the effect of varying redshift is significant. If all bursts are assumed to occur at  $z = 1$  instead, the fluxes increase by a factor 5.6 [19].

It is important to realize, that the results obtained are only valid under these assumptions. Should any of the assumptions later turn out to be unreasonable, this might have large impact on the outcome.

### 6.2.5 Secondary photohadronic interactions and kaon decay

Radiation escaping one shell could in principle interact in another. Although definitely possible, this contribution will be suppressed. Radiation will spend a large fraction of time in between shells, where the probability of photohadronic reaction is negligible. Furthermore, any large amount of neutrino production requires a proton field extending to very high energies. Protons are accelerated at the shock front in the collisions between shells. The extremely energetic protons created in this way will very quickly cool due to synchrotron cooling, as can be seen from equation (4.8), and photons reaching a new shell will not have any high energy protons to interact with. An effect could possibly come from the excess amount of photons from previous collisions in a shell that is just undergoing collision. However, the density of forward traveling photons will decrease the further out the radiation reaches. It turns into a weighting of two different aspects: Radiation from shell collisions at small radii have longer time where secondary photohadronic interaction could occur in other shells, but the density will drop quickly. For shell collisions at larger radii, the radiation density will stay roughly constant, but the time for secondary photohadronic interactions will be shorter. Thus, in both cases, approximating the total pion production as only originating from the initial shell seems justified. With all this in mind, it seems likely that secondary photohadronic interaction plays a very minor roll. Just as with the contribution from subphotospheric collisions and external contributions previously discussed, secondary photohadronic interaction would effectively increase the predicted flux and so figure 6.2 should display a lower bound.

In this work, I have not considered the contribution to the neutrino production from kaon decay. As is evident from Hümmer et al. (2010) [8], this contribution is relatively small. Due to the higher mass of the kaons and therefore shorter lifetime, kaon decay does contribute at the highest neutrino energies after synchrotron cooling is considered. It could also be important for precise flavor ratio predictions [8, 21, 22]. Therefore, this is something that would be interesting to include in a future, more detailed consideration.

Including kaon decay would further increase the neutrino flux.

# Chapter 7

## Conclusion

In this thesis, I have studied five different benchmark GRBs and predicted the neutrino fluxes for each. I have used the multi-shell internal shock model, following a paper published by Bustamante et al. 2016 [17]. The secondary particles have been calculated with a semi-analytical model instead of using a Monte-Carlo software, following a procedure outline by Hümmer et al. 2010 [8]. The purpose was to estimate neutrino all sky fluxes, and to compare these with IceCube's recently published data [4]. With the values  $\epsilon_p = 10/12$ ,  $\epsilon_B = 1/12$ , and  $\epsilon_e = 1/12$  for the energy fractions given to protons, magnetic field, and electrons respectively, and a set, total emitted  $\gamma$ -ray energy of  $10^{52}$ - $10^{53}$  erg, three out of five GRBs resulted in neutrino all sky fluxes above the IceCube 2017 upper limit, set with 90% CL. Taking the average all sky flux for all five GRBs also resulted in a flux above the upper limit. This result speaks against the internal shock model as the main process of GRB energy dissipation, under my current assumptions.

Contributions from below the photosphere, secondary photohadronic interactions, external contributions, and contributions from kaon decays have not been considered. As all these would likely add positively to the flux, my predictions could be seen as lower bounds. However, the results rely heavily on some pre-made assumptions, such as  $\epsilon_p$ ,  $\epsilon_B$ , and  $\epsilon_e$ , redshift  $z$ , and set  $\gamma$ -energies, and by varying these, the fluxes can be decreased below the upper bound.

# Chapter 8

## Acknowledgments

I would like to thank my supervisor Damien Bégué, Postdoc at KTH Royal Institute of Technology, Stockholm, without whom this work would have been much harder and far less enjoyable. With the security of him being present and helpful at all times, I could do a more in depth analysis than I would have otherwise dared. Your encouragement and guidance has really meant a lot, thank you. I would also like to thank my examiner Felix Ryde, Professor at KTH Royal Institute of Technology, Stockholm, for his assistance and flexibility. Finally, I would like to thank my girlfriend whose love and support has been truly invaluable, and my family for always being there for me.

# List of Figures

3.1	Cross sections as function of $\epsilon_r$ for the nine different resonances. The green lines corresponds to $\Delta$ -resonances and the blue to $N$ -resonances. The red line is the total. Figure reproduced from Hümmer et al. (2010) [8]. . . . .	15
3.2	Energy dependence of $\sigma$ for the different production channels. All interactions for each production channel have been summed to create the plot. Figure reproduced from Hümmer et al. (2010) [8]. . . . .	17
3.3	The different production channels contribution to the final $\pi^+$ -distribution. It is clear that all channels are important to correctly predict the shape. Figure reproduced from Hümmer et al. (2010) [8]. . . . .	20
4.1	The effect of synchrotron cooling. The thin lines depict the initial distribution $N_{\pi^+}$ and the thick lines show the particle decay distribution $N_{\pi^+}^{\text{dec}}$ . The figure was obtained with a magnetic field energy density $U_B = 10^{12}$ GeVcm $^{-3}$ and $t_{\text{esc}} = \Gamma l/c = 0.5$ s. . . . .	24
5.1	Initial $\Gamma$ -distribution as a function of $r$ in cm for the five different benchmark GRBs. The central engine is situated at $r = 0$ . . . . .	29
5.2	Shell Lorentz factor $\Gamma$ as a function of radii during the burst evolution of GRB 5. By the end of the burst, all five pulses have smooth, sawtooth shapes with lower average value than originally. . . . .	32
5.3	Burst evolution of quantities for GRB 4. The average mass increases, while the average $\Gamma$ decreases. The average shell speed is $\approx c$ throughout the burst. Collisions radii is relatively evenly spread out, with a tendency to higher energy collisions towards the end. Partial figure inspiration taken from Bustamante et al. (2016) [17]. . . . .	33
5.4	Fractional energy released per collision as a function of observer time for the five GRBs. One can see the similarity to the initial $\Gamma$ -distribution for each burst. Collisions marked with black are subphotospheric, and are thus the earliest collisions in the source frame. Evidently, this does not correspond to an earlier observation time in the OF. . . . .	35
5.5	Energy released in $\gamma$ -rays and neutrinos for each burst. Subphotospheric $\gamma$ -ray energies are shown as well. All GRBs but GRB 3 have strongest neutrino emittance close to the photosphere. Picture inspiration taken from Bustamante et al. (2016) [17]. . . . .	41
6.1	The $\gamma$ and neutrino light curves as observed on earth for $z = 2$ for the five benchmark GRBs. Neutrino light curves include contributions from both $\nu_\mu$ and $\bar{\nu}_\mu$ . Figure inspiration taken from Bustamante et al. (2016) [17]. . . . .	45

6.2	Computed all sky flux of $\nu_\mu + \bar{\nu}_\mu$ from the different GRBs, showed as red lines. The solid lines below are the distributions from the most contributing shell collisions. The black dotted line is the IceCube collaboration's upper limit with 90 % CL [4]. Figure inspiration taken from Bustamante et al. (2016) [17]. . . . .	46
6.3	Predicted all sky fluxes from all five GRBs together with their average, shown as a red dashed line. The IceCube collaboration's 2017 upper limit as well as their 2016 upper limit are shown [4, 17]. . . . .	47
6.4	Plot of how much every hundredth collision above the photosphere contributes to the computed all sky flux. Gives an indication of the shell collision evolution of the burst. The legend indicates collision number, and subphotospheric collisions are marked with an s. . . . .	48
6.5	Neutrino flux as a function of collision radii for the five bursts. Black circles mark subphotospheric collisions while blue circles are superphotospheric collisions. The average photospheric radius has been marked. The red line shows an $r^{-2}$ slope. Figure inspiration taken from Bustamante et al. (2016) [17]. . . . .	49
6.6	Two less extreme initial distribution of $\Gamma$ . . . . .	51
6.7	GRBs 1, 2, and 4 with an upper threshold to the initial shell bulk Lorentz factor, set to $\Gamma^{\text{th}} = 1000$ . The new $\Gamma$ -distributions are shown to the left, with the resulting predicted all sky flux to the right. Although, all fluxes have decreased, they are still above the IceCube 2017 limit [4]. . . . .	52

# List of Tables

5.1	GRB benchmark parameter inputs . . . . .	29
6.1	Less extreme GRB parameter inputs. . . . .	51

# Appendix A

## Justification of arbitrary initial kinetic energy

In the beginning of the simulation, all shells are assigned a common kinetic energy  $E_{\text{kin}}^{\text{iso}}$ . As this initial value is chosen somewhat randomly, it is important to prove that its value does not influence any of the results. In this appendix this will be shown, but proving that  $E_{\text{kin}}^{\text{iso}}$  is directly proportional to the total emitted energy in  $\gamma$ -rays  $E_{\gamma}^{\text{tot}}$ . As  $E_{\gamma}^{\text{tot}}$  is required to equal  $E_{\gamma, \text{set}}^{\text{iso}}$ , the value of  $E_{\text{kin}}^{\text{iso}}$  is indeed irrelevant.

The emitted energy in each collision is calculated as in equation (5.9):

$$E_{\text{coll}, i}^{\text{iso}} = (\Gamma_{k+1} m_{k+1} c^2 + \Gamma_k m_k c^2) - \Gamma_m m_m c^2, \quad (\text{A.1})$$

and the initial masses are chosen as

$$m_{k,0} = \frac{E_{\text{kin}}^{\text{iso}}}{\Gamma_{k,0} c^2}. \quad (\text{A.2})$$

As the initial  $\Gamma$ -values are randomized completely independently of  $E_{\text{kin}}^{\text{iso}}$ , the only thing affected by the choice of initial energy are the initial masses of each shell. As long as these masses always appear together with their respective  $\Gamma$ -value in the emitted energy, it will be directly proportional to  $E_{\text{kin}}^{\text{iso}}$ .

In the case of a first generation collision, between two shells that have not interacted previously, equation (A.1) reduces to

$$E_{\text{coll}, i}^{\text{iso}} = 2E_{\text{kin}}^{\text{iso}} - \Gamma_{m,1} m_{m,1} c^2, \quad (\text{A.3})$$

where the subscript m, 1 indicates a first generation merged shell. The Lorentz factor for the merged shell is calculated as

$$\Gamma_m = \sqrt{\frac{m_{k+1} \Gamma_{k+1} + m_k \Gamma_k}{m_{k+1} / \Gamma_{k+1} + m_k / \Gamma_k}}, \quad (\text{A.4})$$

which, in the case of a first generation collision can be rewritten as

$$\begin{aligned} \Gamma_{m,1} &= \sqrt{\frac{c^2}{c^2} \frac{m_{k+1} \Gamma_{k+1} + m_k \Gamma_k}{m_{k+1} / \Gamma_{k+1} + m_k / \Gamma_k}} = \sqrt{\frac{2E_{\text{kin}}^{\text{iso}}}{E_{\text{kin}}^{\text{iso}} / \Gamma_{k+1}^2 + E_{\text{kin}}^{\text{iso}} / \Gamma_k^2}} = \\ &= \sqrt{\frac{2}{1/\Gamma_{k+1}^2 + 1/\Gamma_k^2}} = \sqrt{\frac{2\Gamma_k^2 \Gamma_{k+1}^2}{\Gamma_k^2 + \Gamma_{k+1}^2}} = \Gamma_k \Gamma_{k+1} C_{k,k+1} \end{aligned} \quad (\text{A.5})$$

where  $C_{k,k+1}$  is a constant independent of  $E_{\text{kin}}^{\text{iso}}$ . As the mass of the merged shells only is the sum of the masses of the parent shells, one can rewrite equation (A.3) as

$$\begin{aligned} E_{\text{coll},i}^{\text{iso}} &= 2E_{\text{kin}}^{\text{iso}} - \Gamma_k \Gamma_{k+1} C_{k,k+1} (m_k + m_{k+1}) c^2 = \\ &E_{\text{kin}}^{\text{iso}} \left( 2 - C_{k,k+1} (\Gamma_k + \Gamma_{k+1}) \right) \propto E_{\text{kin}}^{\text{iso}}. \end{aligned} \quad (\text{A.6})$$

To treat higher generation collisions, we first look at the Lorentz factor of a second generation merged shell:

$$\Gamma_{m,2} = \sqrt{\frac{m_{m,1} \Gamma_{m,1} + m_{k+2} \Gamma_{k+2}}{m_{m,1} / \Gamma_{m,1} + m_{k+2} / \Gamma_{k+2}}}. \quad (\text{A.7})$$

We have already established that

$$\Gamma_{m,1} m_{m,1} c^2 = E_{\text{kin}}^{\text{iso}} C_{k,k+1} (\Gamma_k + \Gamma_{k+1}) = E_{\text{kin}}^{\text{iso}} D_{k,k+1} \propto E_{\text{kin}}^{\text{iso}} \quad (\text{A.8})$$

where  $D_{k,k+1} \equiv C_{k,k+1} (\Gamma_k + \Gamma_{k+1})$  is a constant only dependent on initial Lorentz factor, and therefore still independent of initial energy. Using this, equation (A.6) can be evaluated

$$\begin{aligned} \Gamma_{m,2} &= \sqrt{\frac{D_{k,k+1} + 1}{D_{k,k+1} / \Gamma_{m,1}^2 + 1 / \Gamma_{k+2}^2}} = \Gamma_{m,1} \Gamma_{k+2} \sqrt{\frac{D_{k,k+1} + 1}{\Gamma_{k+2}^2 D_{k,k+1} + \Gamma_{m,1}^2}} = \\ &\Gamma_k \Gamma_{k+1} \Gamma_{k+2} C_{k,k+1} \sqrt{\frac{D_{k,k+1} + 1}{\Gamma_{k+2}^2 D_{k,k+1} + \Gamma_k^2 \Gamma_{k+1}^2 C_{k,k+1}^2}} = \\ &\Gamma_k \Gamma_{k+1} \Gamma_{k+2} C_{k,k+1,k+2}, \end{aligned} \quad (\text{A.9})$$

where  $C_{k,k+1,k+2}$  is nasty constant, but a constant non the less and still independent of  $E_{\text{kin}}^{\text{iso}}$ . As the merged second generation mass is  $m_{m,2} = m_{m,1} + m_{k+2} = m_k + m_{k+1} + m_{k+2}$  the contribution becomes

$$\begin{aligned} \Gamma_{m,2} m_{m,2} c^2 &= E_{\text{kin}}^{\text{iso}} C_{k,k+1,k+2} (\Gamma_k \Gamma_{k+1} + \Gamma_k \Gamma_{k+2} + \Gamma_{k+1} \Gamma_{k+2}) = \\ &E_{\text{kin}}^{\text{iso}} D_{k,k+1,k+1} \propto E_{\text{kin}}^{\text{iso}}, \end{aligned} \quad (\text{A.10})$$

and the energy emitted in a second generation collision becomes

$$E_{\text{coll},i}^{\text{iso}} = (\Gamma_{m,1} m_{m,1} c^2 + \Gamma_{k+2} m_{k+2} c^2) - \Gamma_{m,2} m_{m,2} c^2 \propto E_{\text{kin}}^{\text{iso}}. \quad (\text{A.11})$$

Higher generation  $\Gamma$ -factors behaves in the same way: it can ultimately be rewritten as a product of all initial  $\Gamma$ -factors from previous collisions multiplied by a constant, and as these  $\Gamma$ -factors always appears together by the mass, which is simply a sum of all previous shells' masses, they are proportional to the initial choice of kinetic energy. Putting a requirement on the total emitted  $\gamma$ -radiation thus renders the choice of  $E_{\text{kin}}^{\text{iso}}$  irrelevant. This can be tested by putting  $E_{\text{kin}}^{\text{iso}} = 1$  or  $E_{\text{kin}}^{\text{iso}} = 10^{100}$ , which yields no difference in output.

One very important thing to observe however, is that the photospheric radius is proportional to the mass ejection rate  $\dot{M}$ . The photospheric radius must therefore be scaled together with the output energies.

# Bibliography

- [1] G. Schilling. *Flash! The hunt for the biggest explosions in the universe*, 2<sup>nd</sup> edition, Cambridge University Press: (2002).
- [2] C. Kouveliotou, C. A. Meegan, G. J. Fishman, N. P. Bhat, M. S. Briggs, T. M. Koshut W. S. Paciesas, and G. N. Pendleton. *Identification of two classes of gamma-ray bursts*, The Astrophysical Journal: 413, L101-L104; (1993).
- [3] A. Pe'er. *Physics of gamma-ray bursts prompt emission*, Advances in Astronomy - Hindawi publication company: 2015, 1-37; (2015).
- [4] M. G. Aartsen et al. (IceCube collaboration) *Extending the search for muon neutrinos coincident with gamma-ray bursts in IceCube data*, arXiv:astro-ph/1702.06868; (2017).
- [5] D. L. Meier, S. Koide, and Y. Uchida. *Magnetohydrodynamic Production of Relativistic Jets*, Science: 291, 84-92; (2001).
- [6] S. Kobayashi, T. Piran, and R. Sari. *Can internal shocks produce the variability in GRBs?*, The Astrophysical Journal: 490, 92; (1997).
- [7] K. A. Olive et al. (Particle Data Group) *Review of particle physics*, Chinese Physics C: 38, 9; (2014).
- [8] S. Hümmer, M. Rügner, F. Spanier, and W. Winter. *Simplified models for photohadronic interactions in cosmic accelerators*, The Astrophysical Journal: 721, 630-652; (2010).
- [9] A. Mücke, Ralph Engel, J.P. Rachen, R.J. Protheroe, and Todor Stanev. *Monte Carlo simulations of photohadronic processes in astrophysics*, Computer Physics Communications: 124, 290-314; (2000).
- [10] K. A. Olive et al. (Particle Data Group), *Hadron(photon)-hadron(photon) collisions*, Chinese Physics C: 38, 090001; (2014).
- [11] E. Waxman and J. Bahcall. *High Energy Neutrinos from Cosmological Gamma-Ray Burst Fireballs*, arXiv:astro-ph/9701231v1; (1997).
- [12] P. J. Mohr, B.N. Taylor, and D. B. Newell. *CODATA Recommended Values of the Fundamental Physical Constants: 2010*, Reviews of Modern Physics: 84, 1527; (2012).

- [13] P. Lipari, M. Lusignoli, and D. Meloni. *Flavor composition and energy spectrum of astrophysical neutrinos*, Physical Review D: 75; 123005; (2007).
- [14] T. Hartman. *Neutrino mixing*, Lecture notes: (2003). [https://www.princeton.edu/physics/undergraduate-program/junior-matters/JP%20Samples/hartman\\_may2003.pdf](https://www.princeton.edu/physics/undergraduate-program/junior-matters/JP%20Samples/hartman_may2003.pdf).
- [15] W. Winter. *Lectures on neutrino phenomenology*, Nuclear Physics B: 203-204, 45-81; (2010).
- [16] C. Patrignani et al. (Particle Data Group). *Neutrino mass, mixing, and oscillations*, Chinese Physics C: 40, 100001; (2016).
- [17] M. Bustamante, K. Murase, and W. Winter. *Multi-messenger light curves from gamma-ray bursts in the internal shock model*, arXiv:astro-ph/1606.02325v2; (2016).
- [18] S. Hümmer, P. Baerwald, and W. Winter. *Neutrino Emission from Gamma-Ray Burst Fireballs, Revised*, Physical Review Letters: 108, 231101; (2012).
- [19] E. L. Wright. *A Cosmology Calculator for the World Wide Web*, The Publications of the Astronomical Society of the Pacific: 118, 850, 1711-1715; (2006). <http://www.astro.ucla.edu/~wright/CosmoCalc.html>
- [20] M. J. Rees and P. Mészáros. *Dissipative photosphere models of gamma-ray bursts and X-ray flashes*, The Astrophysical Journal: 628, 847-852; (2005).
- [21] P. Baerwald, S. Hümmer, and W. Winter. *Systematics in the interpretation of aggregated neutrino flux limits and flavor ratios from gamma-ray bursts*, Astroparticle physics: 35, 508-529; (2012).
- [22] P. Baerwald, S. Hümmer, and W. Winter. *Magnetic field and flavor effects on the gamma-ray burst neutrino flux*, Physical Review D: 83, 067303; (2011).